# Measuring Dust Masses of Protoplanetary Disks in Serpens & L1641/L1647 with ALMA

Luisa F. Zamudio-Ruvalcaba, 1,2 Catherine C. Espaillat, 1,2 Álvaro Ribas, 3 and Enrique Macías 4

<sup>1</sup> Department of Astronomy, Boston University, 725 Commonwealth Avenue, Boston, MA 02215, USA
 <sup>2</sup> Institute for Astrophysical Research, Boston University, 725 Commonwealth Avenue, Boston, MA 02215, USA
 <sup>3</sup> Institute of Astronomy, University of Cambridge, Madingley Road, Cambridge, CB3 0HA, UK
 <sup>4</sup> European Southern Observatory, Karl-Schwarzschild-Str. 2, 85748 Garching bei München, Germany

#### ABSTRACT

Protoplanetary disks are an essential component of the planet-formation process. The amount of dust and gas in the disk constrains the number and size of planets that can form in a system. We analyze 178 T-Tauri stars, 18 in Serpens and 160 in L1641/L1647, and measure their disk dust masses using spectral energy distribution (SED) modeling and multiwavelength data, including 1.3 mm (ALMA band 6) fluxes from the literature. The disk masses calculated in this work are up to  $\sim$ 2 times higher than those previously reported. We conclude that this is because disks may be partially optically thick at millimeter wavelengths while most calculations of the disk mass assume that the disk is optically thin at 1.3 mm. We calculate optical depths at 1.3 and 7 mm for a subset of the Serpens and L1641/L1647 disk sample and show that the vast majority of disks become optically thin at longer millimeter wavelengths; thus, observations at 7 mm (i.e., ALMA band 1) are vital to better characterize disk dust masses.

Keywords: accretion, accretion disks — planets and satellites: formation — protoplanetary disks — T Tauri stars

# 1. INTRODUCTION

Stars form from collapsing molecular cloud cores (Goodman et al. 1993) and, due to angular momentum conservation, develop a disk of gas and dust (i.e., a protoplanetary disk). The total mass of the disk dictates the number of resulting planets and the timescale for the planet formation process (Tychoniec et al. 2020). A common assumption is that protoplanetary disks have a gas-to-dust ratio of 100 (Shu et al. 1987; Birnstiel et al. 2010). Although dust makes up only a small fraction of the disk's mass, it dominates the disk's opacity and tends to be more easily observed than gas. By studying the thermal emission from dust grains, we can infer the dust mass and gain insight into the conditions under which planets form.

Disk dust masses can be calculated with different methods (see Bergin & Williams 2018, for a review), but a common method is using millimeter-wavelength flux measurements. Some of the typical values measured for disk dust masses are  $\sim 0.2-0.4~M_{\oplus}$ , which are insufficient to support ongoing planet formation (see Ansdell et al. 2016; Pascucci et al. 2016; Manara et al. 2018) since it implies a planet formation efficiency rate close to 100% (Mulders et al. 2021). This is called the

"missing mass" problem (also known as the "mass budget" problem), and different solutions have been proposed. Planet formation may start much earlier than previously assumed, even during the first Myr of the disk lifetime (e.g. Najita & Kenyon 2014; Manara et al. 2018; Mulders et al. 2021), which is supported by the detection of disk substructures (e.g. ALMA Partnership et al. 2015; Andrews et al. 2018; Segura-Cox et al. 2020) and the presence of the "missing mass" problem in young regions such as Taurus (1-2 Myr). Alternatively, disk dust masses may be underestimated when using the millimeter flux method, which assumes that the disk is optically thin, whereas disks are unlikely to be optically thin throughout all millimeter wavelengths (Ballering & Eisner 2019; Ribas et al. 2020; Xin et al. 2023; Rilinger et al. 2023). Significant mass may also be "hidden" in optically thick dust traps (Savvidou & Bitsch 2024). Lastly, protoplanetary disks may replenish their material by accreting additional material from their surroundings (e.g. Throop & Bally 2008; Kuffmeier et al. 2017; Ginski et al. 2021).

Here, we use SED modeling to measure dust masses for a sample of disks in the Serpens and L1641/L1647

Table 1. Stellar parameters of the Serpens sample.

Object	Parallax	SpT	$T_{eff}$	$A_v$	$L_*$	$R_*$	$M_*$	Reference
2MASS	mas		K		$L_{\odot}$	$R_{\odot}$	$M_{\odot}$	
J18264598-0344306	$2.21 \pm 0.21$	M1	$3730 \pm 100$	$5.54 \pm 0.13$	$0.04 \pm 0.03$	$0.50 \pm 0.23$	$0.50 \pm 0.28$	4
J18264973-0355596	$2.26 \pm 0.16$	K4	$4800\pm100$	$8.53 \pm 0.03$	$0.20 \pm 0.17$	$0.7 \pm 0.3$	$0.7 \pm 0.4$	4
J18273709-0349385	$2.63 \pm 0.11$	K7	$4234\pm100$	$9.972 \pm 0.028$	$0.10 \pm 0.08$	$0.63 \pm 0.29$	$0.6 \pm 0.4$	4
J18274426-0329519	$2.48 \pm 0.17$	M0	$3890 \pm 100$	$7.85 \pm 0.10$	$0.07 \pm 0.06$	$0.59 \pm 0.27$	$0.6 \pm 0.3$	4
J18274445-0356016	$2.29 \pm 0.07$	F9.5	$6008 \pm 100$	$7.890 \pm 0.019$	$4.21 \pm 0.22$	$1.89 \pm 0.05$	$1.22 \pm 0.04$	4
J18275383-0002335	$2.37 \pm 0.04$	K2	$4900 \pm 500$	$1.000 \pm 0.019$	$2.0\pm1.8$	$2.0\pm1.0$	$1.6\pm0.4$	1
J18281519-0001408	$2.58 \pm 0.22$	M8	$2640 \pm 330$	$2.00 \pm 0.04$	$0.11 \pm 0.07$	$1.6\pm0.6$	$0.12 \pm 0.12$	2
J18290088 + 0029312	$2.37 \pm 0.04$	K7	$4060 \pm 220$	$5.00 \pm 0.09$	$1.0 \pm 0.9$	$2.0\pm0.9$	$1.14 \pm 0.20$	2
J18290394 + 0020212	$2.322 \pm 0.027$	K5	$4400 \pm 300$	$7.00 \pm 0.13$	$5.0 \pm 3.0$	$4.0\pm1.5$	$1.6\pm0.4$	2
J18290935-0203503	$2.02 \pm 0.16$	K6	$4360\pm100$	$9.987 \pm 0.020$	$0.14 \pm 0.11$	$0.7 \pm 0.3$	$0.7 \pm 0.4$	4
J18291969 + 0018030	$2.23 \pm 0.21$	M0	$3850\pm100$	$6.00 \pm 0.11$	$0.6 \pm 0.4$	$1.7\pm0.6$	$0.90 \pm 0.10$	2
J18293084 + 0101071	$2.37 \pm 0.06$	F7	$6290 \pm 120$	$6.17 \pm 0.05$	$2.5\pm2.0$	$1.3\pm0.6$	$1.2\pm0.7$	4
J18294147 + 0107378	$2.33 \pm 0.04$	K5	$4400 \pm 300$	$3.30 \pm 0.06$	$0.9 \pm 0.4$	$1.6\pm0.4$	$0.7 \pm 0.3$	3
J18295360 + 0117017	$1.99 \pm 0.10$	K6	$4200\pm200$	$4.60 \pm 0.08$	$0.52 \pm 0.22$	$1.4\pm0.3$	$0.7 \pm 0.3$	3
J18295820 + 0115216	$2.43 \pm 0.14$	K5.5	$4300\pm200$	$5.50 \pm 0.10$	$0.31 \pm 0.12$	$1.02\pm0.20$	$0.8 \pm 0.4$	3
J18300545 + 0101022	$2.39 \pm 0.22$	M3	$3440\pm100$	$4.41 \pm 0.09$	$0.016 \pm 0.013$	$0.36 \pm 0.17$	$0.37 \pm 0.20$	4
J18300610 + 0106170	$2.37 \pm 0.08$	M0	$3800 \pm 210$	$3.70 \pm 0.07$	$0.51 \pm 0.21$	$1.6\pm0.3$	$0.42 \pm 0.20$	3
J18302240 + 0120439	$2.33 \pm 0.05$	M1	$3630\pm130$	$1.80 \pm 0.03$	$0.26 \pm 0.12$	$1.3\pm0.3$	$0.41 \pm 0.19$	3
J18314416-0216182	$1.99 \pm 0.10$	F5	$6650 \pm 100$	$9.630 \pm 0.027$	$3.6 \pm 0.9$	$1.47 \pm 0.11$	$1.33 \pm 0.08$	4
J18321676-0223167	$1.91 \pm 0.16$	K6	$4409 \pm 100$	$7.27 \pm 0.07$	$0.14 \pm 0.11$	$0.7 \pm 0.3$	$0.7 \pm 0.4$	4
J18321707-0229531	$2.12 \pm 0.22$	K3	$4850\pm100$	$9.13 \pm 0.05$	$0.28 \pm 0.23$	$0.8 \pm 0.4$	$0.8 \pm 0.4$	4
J18370677 + 0011479	$1.89 \pm 0.21$	M1	$3690\pm100$	$5.30 \pm 0.06$	$0.04 \pm 0.03$	$0.50 \pm 0.23$	$0.50 \pm 0.28$	4
J18382267+0023093	$2.22 \pm 0.20$	M4.5	$3187 \pm 100$	$2.06 \pm 0.24$	$0.004\pm0.003$	$0.13 \pm 0.06$	$0.18 \pm 0.1$	4

<sup>\*</sup>All parallax values are from Gaia DR3.  $R_*$  is calculated here using literature values. Additional parameters are obtained from various sources as follows: (1,2,3) spectral type,  $T_{eff}$ ,  $A_v$ ,  $L_*$ , and  $M_*$  are compiled from Oliveira et al. (2009), Oliveira et al. (2013), and Erickson et al. (2015), respectively; (4) spectral type is from Pecaut & Mamajek (2013) using the  $T_{eff}$  available in the literature;  $T_{eff}$  and  $A_v$  are gathered from the derived values from GSP-Phot using BP/RP spectra (Gaia Collaboration et al. 2023). The General Stellar Parametrizer for Photometry (GSP-Phot) derives stellar parameters ( $T_{eff}$ ,  $\log g$ ,  $A_G$ , distance, etc.) from BP/RP spectra down to G=19, assuming all sources are stars. It infers these parameters using Gaia's low-resolution BP/RP spectra, astrometry, and photometry. We refer the reader to consult Gaia Collaboration et al. (2023) and Andrae et al. (2023) for further details on the GSP-Phot methodology.  $L_*$  and  $M_*$  are estimated here using the MassAge code following Hernández et al. (2023). In short,  $L_*$  is calculated using extinction-corrected J magnitudes (Luhman & Esplin 2020), bolometric corrections from Pecaut & Mamajek (2013), and distances derived from parallaxes (Gaia DR3).  $M_*$  is derived using the MIST (Dotter 2016) evolutionary models.

star-forming regions. We focus on disks around T-Tauri stars (TTS) which are pre-main sequence, low-mass (0.08  $\rm M_{\odot} \leq M_{*} \leq 2 \rm M_{\odot}$ ; Joy 1945; Herbig 1962), cool (late spectral types K-M) stars exhibiting photometric variability as well as characteristic emission and absorption lines (e.g.,  $\rm H\alpha$  and Li 6707 Å, respectively). We use ALMA 1.3 mm continuum observations from the Serpens star-forming region (Anderson et al. 2022) and the Orion A cloud in the L1641 and L1647 regions (van Terwisga et al. 2022). We incorporate broad-band photometry and low-resolution *Spitzer* Infrared Spectrograph

(IRS) spectra from CASSIS (Houck et al. 2004). The SED model fitting adopts the technique developed by Ribas et al. (2020), which employs an Artificial Neural Network (ANN) trained with the D'Alessio Irradiated Accretion Disk models (DIAD; D'Alessio et al. 1998, 1999, 2001, 2005, 2006). This paper's structure is as follows: we describe the sample selection in Section 2, we present analysis and results from the SED modeling in Section 3, we discuss our results in Section 4, and finally we provide conclusions in Section 5.

Table 2. Stellar parameters for L1641/L1647.

Object	Parallax	$\operatorname{SpT}$	$T_{eff}$	$A_v$	$L_*$	$R_*$	$M_*$	Reference
2MASS	mas		K		$L_{\odot}$	$R_{\odot}$	$M_{\odot}$	
J05324993-0610456	$2.63 \pm 0.06$	M0.8	$3770 \pm 110$	$0.90 \pm 0.24$	$0.08 \pm 0.23$	-	$0.55 \pm 0.07$	3,4
J05332098-0622333	$2.54 \pm 0.05$	M1	$3742 \pm 100$	$2.1 \pm 0.6$	$0.4 \pm 1.1$	$1.6\pm2.2$	$1.80 \pm 0.22$	3,5,8
J05334160-0606074	$2.44 \pm 0.15$	M3.5	$3378 \pm 100$	$0.17 \pm 0.05$	_	-	_	3,6
J05335945-0621182	$2.65 \pm 0.07$	M4.1	$3210\pm100$	$0.30 \pm 0.08$	$0.09 \pm 0.25$	-	$0.170\pm0.021$	3,4
J05340108-0602268	$2.600 \pm 0.018$	K7.6	$3860 \pm 100$	$0.34 \pm 0.09$	$0.4 \pm 1.0$	$1.4\pm1.9$	$0.68 \pm 0.04$	1,7
J05340495-0623469	$2.61 \pm 0.05$	M4	$3349 \pm 100$	$0.94 \pm 0.21$	$0.2 \pm 1.1$	$1 \pm 4$	$0.35 \pm 0.04$	1,7
J05342043-0631150	$2.42 \pm 0.15$	M5.1	$3060\pm100$	$0.60 \pm 0.16$	$0.06 \pm 0.16$	-	$0.1 \pm 0.012$	1,3,4
J05343096-0558036	$2.32 \pm 0.09$	M5.1	$3100\pm100$	$0 \pm 0.3$	$0.05 \pm 0.14$	_	$0.098 \pm 0.012$	3,4
J05343319-0614287	$2.64 \pm 0.20$	M5.4	$2930 \pm 100$	_	_	_	_	1,3
J05343360-0611194	$2.58 \pm 0.07$	M4.8	$3110\pm100$	$0 \pm 0.3$	$0.06 \pm 0.17$	-	$0.120\pm0.015$	3,4

<sup>\*</sup> All parallax values are from Gaia DR3.  $R_*$  is calculated here using literature values. Additional parameters are obtained from various sources as follows: (1,2) spectral types come from Hsu et al. (2012) and Hsu et al. (2013), respectively; (3) spectral type (or  $T_{eff}$ ) is from Pecaut & Mamajek (2013) using  $T_{eff}$  (or spectral type) from the literature; (4) spectral type or  $A_v$ ,  $L_*$ , and  $M_*$  are sourced from Fang et al. (2009, 2013, 2018); (5)  $T_{eff}$  was taken from APOGEE-2 DR17 (Abdurro'Uf & et al. 2023); (6)  $T_{eff}$  and  $A_v$  are gathered from the derived values from GSP-Phot using BP/RP spectra (Gaia Collaboration et al. 2023) (see Table 1 caption for further details on GSP-Phot); (7) Serna et al. (2023) provides  $T_{eff}$ ,  $A_v$ ,  $L_*$ , and  $M_*$ ; (8)  $A_v$ ,  $L_*$ , and  $M_*$  is from Roman-Zuniga et al. (2023); (9) Kim et al. (2016) gives spectral type or  $A_v$ ,  $L_*$ , and  $M_*$ ; (10) da Rio et al. (2016) provides  $A_v$ ,  $L_*$ , and  $M_*$ ; (11)  $T_{eff}$  or  $L_*$ ,  $R_*$  are gathered from Gaia DR2 (Gaia Collaboration et al. 2018) estimates for temperature from Apsis-Priam and radius/luminosity estimates from Apsis-FLAME, respectively (see Andrae et al. (2018) and Bailer-Jones et al. (2013) for more details regarding the stellar parameter estimation with the Apsis data processing pipeline); (12) stellar parameters correspond to those adopted for the objects analyzed in Rilinger et al. (2023). This table is published in its entirety in the machine-readable format. A portion is shown here for guidance regarding its form and content.

# 2. SAMPLE SELECTION

The sample used in this work comprises TTS with disks in the Serpens, L1641, and L1647 regions. (Sub)millimeter observations are necessary to constrain the disk's dust mass, so we compiled our sample using (sub)millimeter surveys of these regions. We selected our Serpens sample from Anderson et al. (2022), a continuum and  ${}^{12}CO$  (J=2-1) line survey spread over an area of  $\sim 10$  square degrees in Serpens which observed 320 objects studied by the Spitzer From Molecular Cores to Planet-Forming Disks C2D Overview (hereafter c2d; Evans et al. 2003, 2009) and the Gould Belt Survey (Dunham et al. 2015). The L1641 and L1647 sample is obtained from the Survey of Orion Disks with ALMA (SODA; van Terwisga et al. 2022), which observed 873 protoplanetary disks identified by *Spitzer* (Evans et al. 2009; Dunham et al. 2015). Both Anderson et al. (2022) & van Terwisga et al. (2022) use the ALMA 1.3 mm band (centered at 241.1 GHz and 225 GHz, respectively).

The original sample of 320 Serpens sources (Anderson et al. 2022) comes down to 23 objects, and the 873 L1641/L1647 sources (van Terwisga et al. 2022) to 188

objects after considering several criteria. They must belong to the Serpens or L1641/L1647 star-forming regions and be identified as Class II YSOs. Each source must have been detected by ALMA and have at least two 2MASS measurements, two mid-infrared (WISE or c2d) measurements, and one (sub)millimeter (ALMA) measurement. Sources known to be transitional disks (TDs), exhibit flat spectra, or belong to binary or multiple systems were excluded. Additionally, the sources must not have a (sub)mm measurement within 2".5 of another (sub)mm detection of at least  $3\sigma$ . Only sources with ALMA detections of at least  $3\sigma$  were included. To ensure reliable astrometric data (e.g., parallax), the selected sources must display good Gaia astrometric quality. Finally, all sources must be classified as T Tauri stars and have stellar parameters available in the literature. The  $T_{eff}$ ,  $R_*$ ,  $M_*$ , and parallaxes listed in Tables 1 and 2 are used in the SED fitting as described in Section 3.2.1 and 3.2.2, and the rest of the parameters are listed for completeness. We note that for  $T_{eff}$ , we adopted an uncertainty of 100 K for those objects with reported uncertainties below 100 K, following Ribas et al. (2020).

We refer the reader to Appendix A for a more detailed review of the selection criteria. This results in an overall sample of 211 objects.

# 3. ANALYSIS AND RESULTS

Below, we compile the SEDs for the 211 sources in Serpens, L1641, and L1647 selected in Section 2. A subset of 41 sources from L1641 were modeled in Rilinger et al. (2023) and we incorporate their model results here. We provide an overview of the SED modeling methodology using the ANN developed by Ribas et al. (2020), which applies a Bayesian approach and is trained with DIAD models. We end with the resulting model fits and further reduce our sample to 178 sources (18 from Serpens and 160 from L1641/L1647) based on the quality of the fits.

#### 3.1. *SEDs*

We compile the SEDs using multiwavelength photometry gathered for each object from the Vizier catalog access tool (Ochsenbein et al. 2000), using a search radius of 2". Table 3 lists all photometry sources used. We also include low-resolution *Spitzer IRS* spectra for each object, if available, which were obtained from the Combined Atlas of Sources with *Spitzer IRS* Spectra (CASSIS; Lebouteiller et al. 2011).

# 3.2. SED modeling

To fit our objects' SEDs, we use a model that relies on the ANN developed by Ribas et al. (2020), and trained on the D'Alessio Irradiated Accretion Disk models (DIAD; D'Alessio et al. 1998, 1999, 2001, 2005, 2006). We follow a Bayesian approach as detailed in Ribas et al. (2020) and Xin et al. (2023) to estimate our sample of disks' posterior probability density functions based on their respective SEDs.

# 3.2.1. The model

The work by Ribas et al. (2020) presents a novel approach to fit samples of protoplanetary disks, combining physically motivated models with a neural network to speed the process of model fitting; the ANN takes a few milliseconds to evaluate the SEDs, compared to the 1-2 hours that the DIAD models require, which, as previously discussed, makes the model fitting considerably time-consuming for large samples. We direct the reader to Section 4 and Figure 2 of Ribas et al. (2020) for a detailed description of the model and a summary of the steps, which are also summarized below.

The ANN comprises two artificial neural networks:  $ANN_{SED}$  for SED estimates and  $ANN_{diskmass}$  for disk

mass estimates. The ANN provides SED estimates based on input parameters. Each of the models computed in the fitting procedure goes through the following steps:

- 1. Stellar age and  $M_*$  are taken as free parameters of the model, and for each pair,  $T_*$  and  $R_*$  are estimated from the MESA Isochrones and Stellar Tracks (MIST; Paxton et al. 2011, 2013, 2015; Dotter 2016; Choi et al. 2016). This process ensures that our model explores combinations of stellar age,  $M_*$ ,  $R_*$ , and  $T_*$  that are physically realistic, which is required because these parameters are used to evaluate the SEDs. Likewise,  $L_*$  is not a free parameter in the model but is derived from MIST. We point the reader to Section 3.2.2 for more details about how literature information about the stellar parameters is used in the modeling.
- 2. The ANN uses  $M_*$ ,  $T_*$ , and  $R_*$  as well as the following disk and dust parameters:
  - Mass accretion rate  $\dot{M}$
  - Disk viscosity  $\alpha$  (adimensional and following Shakura & Sunyaev 1973).
  - Dust settling  $\epsilon$  (adimensional)
  - Maximum grain sizes in the disk atmosphere  $a_{max,upper}$  and midplane  $a_{max,midplane}$
  - Disk size  $R_{disk}$
  - Inclination i
  - Dust sublimation temperature  $T_{wall}$
  - Scaling factor of the inner wall  $z_{wall}$

Consequently, the ANN generates the corresponding SED for a reference distance of 100 pc in the absence of extinction to the source. We refer the reader to the DIAD papers (D'Alessio et al. 1998, 1999, 2001, 2005, 2006) for further details on these disk and dust parameters.

3. The SED output is scaled to the source's distance (based on the corresponding parallax, which is another free parameter in our model) and reddened by  $A_v$ , applying the McClure (2009) extinction law (following Ribas et al. 2017). Here,  $A_v$  denotes the interstellar extinction and does not include the self-extinction contributed by the disk, which is already incorporated in DIAD.

Some caveats need to be taken into account for this methodology. As discussed in Section 2, the objects that

**Table 3.** Photometry sources for the sample

SED filter	Wavelength $[\mu m]$	Instrument	Reference
SDSS:u	0.352	APOGEE-2	Ahumada et al. (2020)
Johnson B	0.4361	AAVSO	Henden et al. (2016)
POSS-II:J	0.468	GSC2.3	Lasker et al. (2008)
PS1:g	0.477	PAN-STARRS	Chambers et al. (2016)
SDSS:g	0.482	APOGEE-2	Ahumada et al. (2020)
$G_{BP}$	0.504	Gaia DR3	Gaia Collaboration et al. (2023)
Johnson V	0.5448	AAVSO	Henden et al. (2016)
G	0.582	Gaia DR3	Gaia Collaboration et al. (2023)
PS1:r	0.613	PAN-STARRS	Chambers et al. (2016)
SDSS:r	0.625	APOGEE-2	Ahumada et al. (2020)
POSS-II:F	0.640	GSC2.3	Lasker et al. (2008)
$G_{RP}$	0.726	Gaia DR3	Gaia Collaboration et al. (2023)
PS1:i	0.748	PAN-STARRS	Chambers et al. (2016)
SDSS:i	0.763	APOGEE-2	Ahumada et al. (2020)
POSS-II:i	0.784	GSC2.3	Lasker et al. (2008)
PS1:z	0.865	PAN-STARRS	Chambers et al. (2016)
SDSS:z	0.902	APOGEE-2	Ahumada et al. (2020)
PS1:y	0.960	PAN-STARRS	Chambers et al. (2016)
W3	1.16	WISE	Cutri et al. (2021)
J	1.24	2MASS	Skrutskie et al. (2006)
H	1.65	2MASS	Skrutskie et al. (2006)
$K_s$	2.16	2MASS	Skrutskie et al. (2006)
W4	2.21	WISE	Cutri et al. (2021)
W1	3.35	WISE	Cutri et al. (2021)
IRAC:3.6	3.55	Spitzer	Evans et al. (2003)
IRAC:4.5	4.49	Spitzer	Evans et al. (2003)
W2	4.6	WISE	Cutri et al. (2021)
IRAC:5.8	5.73	Spitzer	Evans et al. (2003)
IRAC:8.0	7.87	Spitzer	Evans et al. (2003)
MIPS:24	23.7	Spitzer	Evans et al. (2003)
Herschel:70	70	Herschel	Marton et al. (2017)
Herschel: 100	100	Herschel	Marton et al. (2017)
Herschel: 160	160	Herschel	Marton et al. (2017)
Band 6	1333	ALMA	Anderson et al. (2022); van Terwisga et al. (2022)

make up our sample must comply with specific selection criteria. Some physical properties remain fixed (e.g. dust composition, gas-to-dust ratio) or not considered in the modeling (i.e. the presence of substructures in the disk). Refer to Ribas et al. (2020) for an in-depth discussion of the caveats of this methodology. Most importantly, this sample is only made up of sources detected in the (sub)mm range. This would bias the analysis towards massive disks and underrepresented low-mass disks, which are less luminous, smaller in radius, and thus harder to detect.

#### 3.2.2. Markov Chain Monte Carlo (MCMC)

We implement a Bayesian analysis framework as a Markov Chain Monte Carlo (MCMC) fitting process to probe the large parameter space and estimate posterior distributions for the model parameters. Following Rilinger et al. (2023), we adopted the likelihood functions from Ribas et al. (2020) and Xin et al. (2023), as well as the ptemcee (Vousden et al. 2016) parallel-tempering version of the emcee MCMC code (Foreman-Mackey et al. 2013). Our photometry points were divided into two groups:

- critical: includes 2MASS and ALMA photometry (Anderson et al. 2022)
- general: includes all other photometry

The division allows us to provide further weight to the 2MASS and ALMA photometry, which are vital for accurately scaling the stellar photosphere and calculating the disk mass, respectively. Four standard Gaussian likelihood functions are used, each for the critical photometry data, the spectral data (i.e., IRS Spectra), the  $T_*$ , and the  $R_*$ . To account for possible systematic uncertainties that may be present in the data from different instruments, Xin et al. (2023) scaled all of the uncertainties in the flux densities according to the free parameter, f. Some photometric points may differ significantly from the rest of the SEDs and are problematic in the fitting process. Xin et al. (2023) employed a mixture model approach, following the methodology described by Hogg et al. (2010). This approach was applied to the general photometry data, enabling the overall likelihood to incorporate information from both the photometric and spectral data. We note that Gaussian priors are used for the  $M_*$  and parallaxes listed in Tables 1 and 2 to represent pre-existing information on these parameters, using their values as the centers and their uncertainties as the standard deviations, while flat priors are used when literature values are absent (e.g., inclination). We refer the reader to consult Xin et al. (2023) and Rilinger et al. (2023) for more details.

Hence, the model has 13 free parameters: Stellar age,  $M_*$ , DIAD parameters (i.e.  $\dot{M}$ ,  $\alpha$ ,  $\epsilon$ ,  $a_{max,upper}$ ,  $a_{max,midplane}$ ,  $R_{disk}$ , i,  $T_{wall}$ , and  $z_{wall}$ ), parallax, and  $A_{v}$  of the source, all of them determined using the MCMC fitting process. Finally, since we are compiling the SEDs from multiple catalogs, it is likely that some of the data points may be affected by undetected issues (i.e., source blending, saturation, artifacts). In order to reduce the impact of these outliers on the modeling, we include four additional parameters to mitigate the influence of such uncertainties during the fitting process: three of these account for possible outlier photometric points, and one, the f parameter, accounts for potential systematic uncertainties inherent in the data acquired from different instruments. This results in a total of 17 free parameters, which are varied during the fitting to compute posterior probability distributions.

For an in-depth exploration and discussion of the MCMC process on which the ANN operates, we refer to the following works by Ribas et al. (2020), Rilinger et al. (2023), and Xin et al. (2023).

# 3.3. Model results

Figures 1 & 2 display the modeling results for Serpens and L1641/L1647, respectively. We identified successful and unsuccessful model fits for both samples; see Rilinger et al. (2023) for examples and further discussion on unsuccessful model fits.

For the Serpens sample, six sources have unsuccessful fits, which may be due to incorrect stellar parameters, unknown substructures, or the potential presence of companions, as well as processes not taken into account by the methodology of Ribas et al. (2020). These include the following sources: 2MASS J18273709-0349385 (model does not fit the *Spitzer* photometry), 2MASS J18290394+0020212 (exhibits variability between the infrared IRS spectra and Spitzer photometry), 2MASS J18290935-0203503 (model does not fit infrared photometry, Spitzer and WISE, as well as the millimeter photometry), 2MASS J18370677+0011479 (the model does not fit the 2MASS photometry and infrared structure of the SED), 2MASS J18382267+0023093 (the model does not fit the infrared structure of the SED), 2MASS J18373580+0019053 (the photometry has very large scatter and is difficult to fit). Thus, the Serpens sample consists of 18 successfully modeled disks.

For the L1641/L1647 region, 28 sources were discarded based on failed fits. We arrive at a sample of 160 successfully modeled sources in L1641/L1647.

Results from the model fits for individual sources and ensemble distributions are shown in Figures 3 and 4 for Serpens and L1641/L1647, respectively. Similarly, Table 4 display the median values and corresponding errors (calculated from the 16th and 84th percentiles of the distribution) for the posterior distributions of stellar and disk parameters, respectively, obtained from the model fitting for Serpens. Meanwhile, Table 5 lists those for L1641/L1647. An assessment of the consistency between the stellar parameters  $(M_*, R_*, \text{ parallax}, \text{ and } T_{\text{eff}}; \text{ as}$ listed in Tables 1 and 2, and their respective posterior distributions in Tables 4 and 5) is conducted to validate the robustness of the ANN fitting methodology. We refer the reader to Appendix B for a more detailed review of this validation procedure. The corresponding corner plots generated from the MCMC process for all 178 disks are hosted within the designated Zenodo repository.

Figures 3 & 4 show some similarities in trends of the physical parameters. Disk mass depends on the disk viscosity  $(\alpha)$  and the mass accretion rate  $(\dot{M})$ , as both parameters determine the surface density profile of the disk  $\Sigma \propto \dot{M}/\alpha$ . These parameters are relatively well-constrained for both samples compared to the other parameters. The  $R_{disk}$  and  $a_{max,midplane}$  (i.e., the maximum grain size in the midplane) are not well constrained, consistent with the results of Ribas

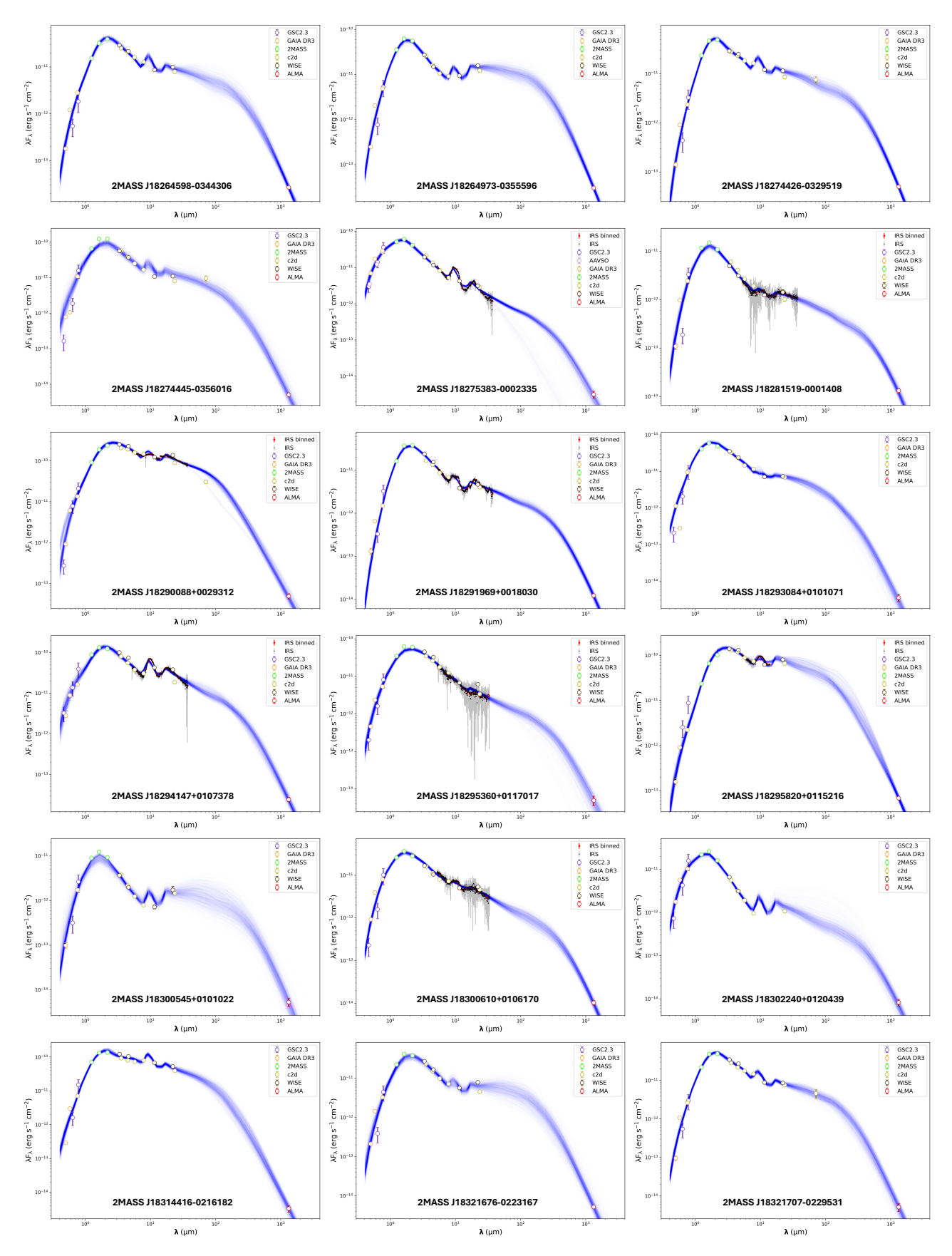


Figure 1. The observed SEDs and models for the 18 successfully fitted protoplanetary disks in our Serpens sample. The blue lines show 1000 randomly selected models from the posterior distributions. The models are reddened using McClure (2009) extinction law and the extinction values gathered from the MCMC fitting process (see Section 3.2.2). Photometry labels are detailed in Table 3. Spitzer data is labeled as c2d. The complete figure set (18 images) is available in the online journal.

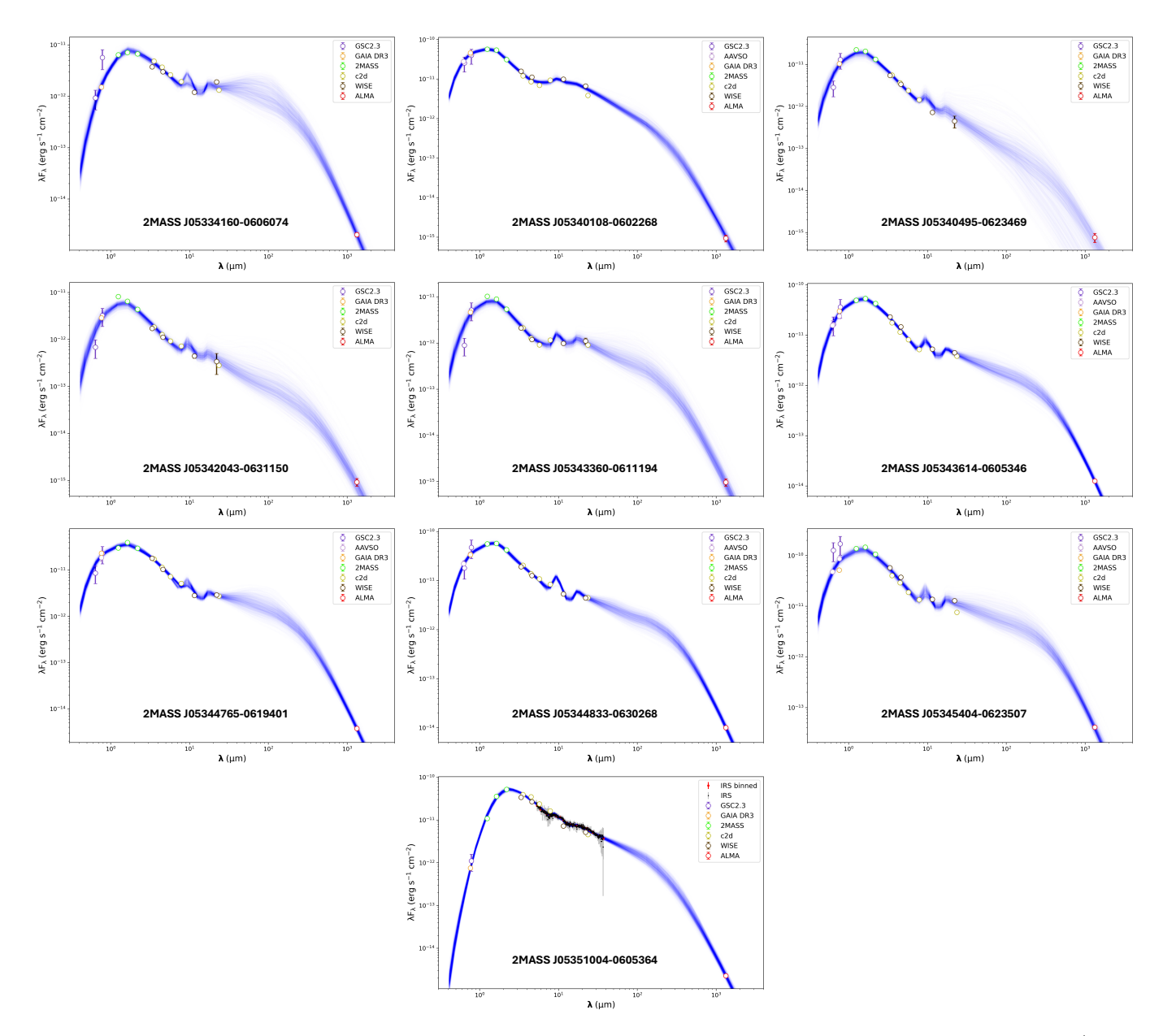


Figure 2. The observed SEDs and successfully fitted models for the first 10 of the 160 protoplanetary disks in our L1641/L1647 sample. The blue lines show 1000 randomly selected models from the posterior distributions. The models are reddened using McClure (2009) extinction law and the extinction values gathered from the MCMC fitting process (see Section 3.2.2). Photometry labels are detailed in Table 3. Spitzer data is labeled as c2d. The complete figure set (119 images) is available in the online journal. The additional SEDs for the 41 L1641 objects can be consulted in Rilinger et al. (2023).

et al. (2020) and Xin et al. (2023), which use the same method. The  $\epsilon$  parameter, which measures the dust settling in the disk, shows a preference towards lower values in both samples (i.e.,  $\epsilon < 10^{-2}$ ), indicating that the studied disk populations have already undergone significant settling. This agrees with previous works where high degrees of dust settling are observed in L1641/L1647 (Grant et al. 2018; Großschedl et al. 2019) and Serpens (Liu et al. 2023). For  $a_{max,upper}$ , the maximum grain size in the upper layers of the disk, some objects in both samples are well-constrained while others are not. This may be due to the availability of IRS spectra for each object, as the size of the upper layer dust grains is determined from mid-IR, in particular from the shape of the silicate feature at 10-20  $\mu$ m. This reinforces the importance of having mid-IR spectra to better constrain dust population characteristics in the disk. Further discussion of a similar analysis of these posterior distributions for different populations can be found in Ribas et al. (2020) for Taurus-Auriga and in Xin et al. (2023) for Lupus.

# 4. DISCUSSION

Here, we discuss the importance of considering optical depth when calculating disk dust masses, particularly for massive disks, which tend to be more affected. We follow by comparing our dust mass measurements (based on SED modeling) with those from the literature (based on mm fluxes; Anderson et al. 2022; van Terwisga et al. 2022), and show that our values become more discrepant with the values from the literature as we move toward more massive disks. Next, we compare Serpens and L1641/L1647 to 10 other star-forming regions with ages less than 10 Myr and confirm that both samples follow the observed trends for disk dust mass in other regions. We conclude by discussing how our dust masses are greater than those calculated from mm fluxes, but this does not fully solve the "missing mass" problem as our values are still lower when compared to exoplanet systems.

# 4.1. The importance of optical depth when deriving disk masses

We compare our sample's model-derived disk dust masses with those found in the literature in Figure 5. The literature values in Figure 5 are from Anderson et al. (2022) & van Terwisga et al. (2022), and are recalculated using *Gaia* DR3 parallaxes and using the Hildebrand (1983) equation:

$$M_d = \frac{F_{\nu} d^2}{\kappa_{\nu} B_{\nu}(T_d)} \tag{1}$$

where  $M_d$  is the dust mass in the disk;  $F_{\nu}$  is the millimeter flux density at the observing frequency, here 1.3 mm (241 GHz);  $\kappa_{\nu}$  is the dust opacity coefficient at the observing frequency, and following Anderson et al. (2022), we adopt  $\kappa_{\nu} = (\nu/100 \text{ GHz})$  (see Beckwith et al. 1990) resulting in 2.41  $cm^2g^{-1}$  while assuming  $\beta=1$ ;  $B_{\nu}(T_d)$  is the Planck function evaluated at the dust temperature  $T_d$ , which is typically assumed to be constant with a value of  $T_d=20~K$  for a Class II object (Andrews & Williams 2005; Ansdell et al. 2016, 2017; Ruíz-Rodríguez et al. 2018; Cazzoletti et al. 2019; Williams et al. 2019; Anderson et al. 2022); d is the distance calculated from Gaia DR3 parallaxes. The recalculated disk dust masses for Serpens and L1641/L1647 are listed in Tables 6 & 7, respectively.

In Figure 5, the calculated disk dust masses from the literature are consistently lower than in this work, especially when assuming a constant temperature profile. We find that, on average, our masses are a factor of about 2.0 higher for both Serpens and L1641/L1647. In most cases, the discrepancy is even higher for the higher-mass objects.

The discrepancy between disk dust masses when using the Hildebrand (1983) equation versus SED modeling has been reported in other works. Ballering & Eisner (2019) find that the masses derived with their SED modeling are  $\sim 1-5$  higher. The same is seen in Ribas et al. (2020), where the estimated  $M_{dust}$  from SED modeling is  $\sim 3$  higher than that reported in Andrews et al. (2013). Other works such as Macías et al. (2021); Liu et al. (2022) find masses  $\sim 3-5$  higher, respectively. Recent work by Xin et al. (2023); Rilinger et al. (2023) shows that the SED modeling-derived masses are, respectively,  $\sim 1.5-6 \& \sim 1.5-5$  times higher than those obtained from the literature. Using values from Rilinger et al. (2023) and this work for the Serpens and L1641/L1647 samples, Figure 6 compares all 12 regions and shows the mass ratio between disk mass derived from SED modeling and those calculated from literature fluxes. The discrepancy factor, given as  $M_{dust,DIAD}/M_{dust,lit}$ , has a median of  $\sim 1.74$  for all regions and shows a slight increase toward the most massive disks. For younger regions (i.e., <2 Myr; Ophiuchus, Taurus, Cha II, L1641/L1647, Serpens, and Lupus) the discrepancy factor is greater than the populations' average (i.e., 2.0), while for older regions (i.e., >2Myr; Cha I, IC 348, Corona Australis,  $\sigma$  Ori,  $\lambda$  Ori, and Upper Sco) the discrepancy factor is lower (i.e., 1.2). Taurus has the biggest discrepancy factor (4.09), and Upper Sco has the lowest (0.72). It is important to note

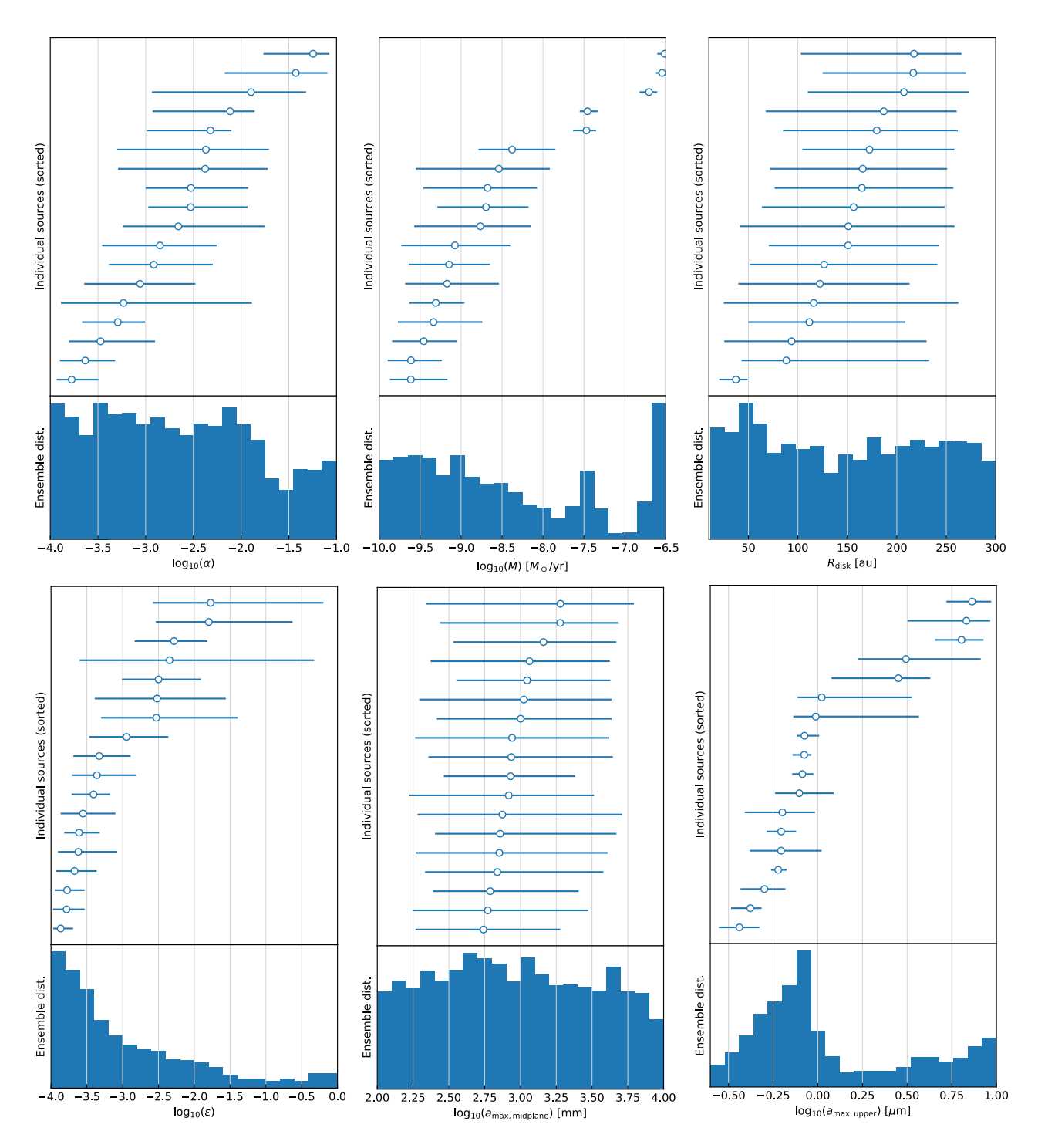


Figure 3. Posterior distributions of the individual 18 successfully modeled sources of the Serpens sample (top panels) and ensemble distribution (bottom panels) for the following parameters (from top left to bottom right):  $\alpha$  (disk viscosity),  $\dot{M}$  (mass accretion rate),  $R_{disk}$  (outer disk radius),  $\epsilon$  (dust settling),  $a_{max,midplane}$  (maximum grain size in the midplane),  $a_{max,upper}$  (maximum grain size in the upper layers of the disk). The error bars denote the 16th and 84th percentiles; the bottom panels' histograms use 20 bins.

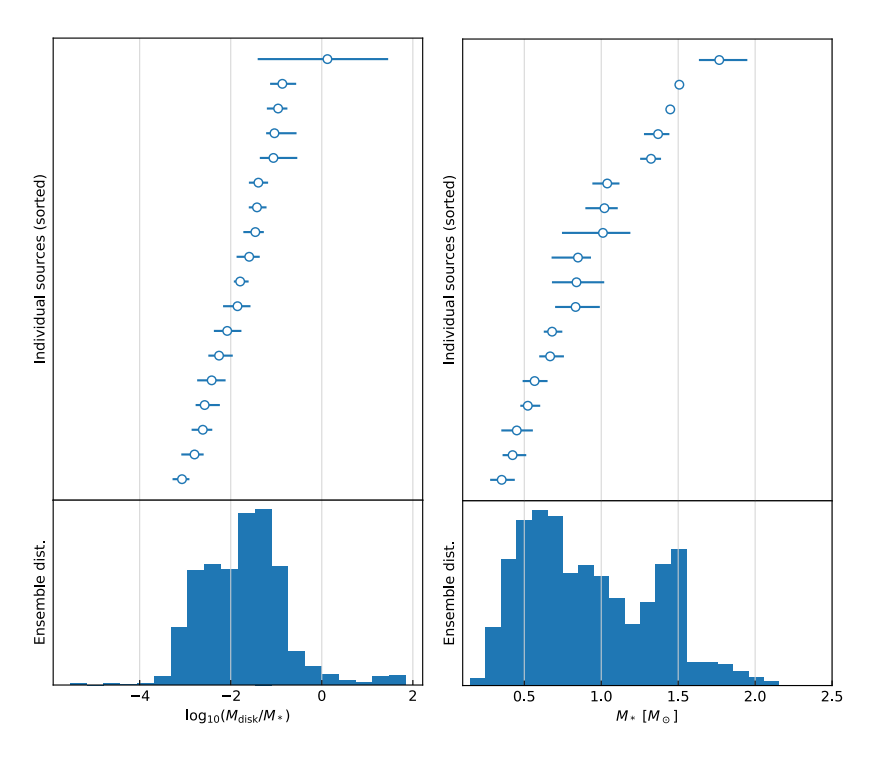


Figure 3. (Continued). Posterior distributions of the individual 18 successfully modeled sources of the Serpens sample (top panels) and ensemble distribution (bottom panels) for the following parameters (from left to right):  $M_{disk}/M_*$  (disk mass fraction to host star mass),  $M_*$  (host star mass).

Table 4. Posteriors for Serpens stellar and disk parameters

Object	$T_{eff}$	Radius	Mass	Parallax	$log_{10}(\dot{M})$
2MASS	K	$R_{\odot}$	$M_{\odot}$	mas	$M_{\odot}/yr$
J18264598-0344306	$3720^{+80}_{-90}$	$1.02^{+0.14}_{-0.09}$	$0.54^{+0.08}_{-0.07}$	$2.3^{+0.2}_{-0.2}$	$-7.50^{+0.13}_{-0.12}$
J18264973-0355596	$4800^{+100}_{-100}$	$1.93^{+0.17}_{-0.16}$	$1.37^{+0.08}_{-0.09}$	$2.48^{+0.14}_{-0.14}$	$-8.7^{+0.5}_{-0.7}$
J18274426-0329519	$3880^{+90}_{-90}$	$1.25^{+0.21}_{-0.16}$	$0.66^{+0.08}_{-0.08}$	$2.58^{+0.17}_{-0.17}$	$-7.50^{+0.12}_{-0.13}$
J18274445-0356016	$5860^{+60}_{-50}$	$1.85^{+0.04}_{-0.04}$	$1.450^{+0.013}_{-0.012}$	$2.31^{+0.07}_{-0.07}$	$-9.1^{+0.7}_{-0.6}$
J18275383-0002335	$4400^{+300}_{-300}$	$1.57^{+0.15}_{-0.12}$	$1.03^{+0.16}_{-0.27}$	$2.36^{+0.04}_{-0.04}$	$-9.6^{+0.5}_{-0.3}$

$log_{10}(lpha)$	$log_{10}(\epsilon)$	$R_{disk}$	$\mathbf{a}_{\mathrm{max,\; upper}}$	$\mathbf{a}_{\mathrm{max,\ midplane}}$	$T_{wall}$	Inclination	$M_{dust}$
		au	$\mu\mathrm{m}$	mm	K	$\deg$	$M_{\oplus}$
$-2.1^{+0.3}_{-0.9}$	$-2.4^{+1.3}_{-0.9}$	$100^{+120}_{-60}$	$0.86^{+0.21}_{-0.09}$	$1000^{+4000}_{-810}$	$1400^{+50}_{-40}$	$59^{+6}_{-12}$	$200^{+700}_{-90}$
$-3.1^{+0.6}_{-0.6}$	$-2.9^{+0.6}_{-0.5}$	$150^{+100}_{-93}$	$0.51^{+0.22}_{-0.14}$	$1000^{+3000}_{-700}$	$1420^{+50}_{-50}$	$20^{+30}_{-10}$	$70^{+50}_{-20}$
$-2.3^{+0.2}_{-0.5}$	$-3.3^{+0.5}_{-0.4}$	$169^{+92}_{-100}$	$0.62^{+0.07}_{-0.06}$	$1000^{+3000}_{-800}$	$1440^{+40}_{-40}$	$59^{+6}_{-8}$	$300^{+200}_{-90}$
$-2.6^{+0.7}_{-0.6}$	$-3.6^{+0.6}_{-0.3}$	$180^{+80}_{-100}$	$0.76^{+0.50}_{-0.18}$	$1000^{+3000}_{-500}$	$1420^{+50}_{-50}$	$22^{+21}_{-9}$	$11^{+8}_{-4}$
$-2.9^{+0.6}_{-0.4}$	$-3.7^{+0.3}_{-0.2}$	$180^{+90}_{-100}$	$0.36^{+0.10}_{-0.07}$	$1000^{+4000}_{-1100}$	$1400^{+50}_{-50}$	$68^{+1}_{-4}$	$12^{+10}_{-6}$

NOTE—This table is published in its entirety in the machine-readable format. A portion is shown here for guidance regarding its form and content.

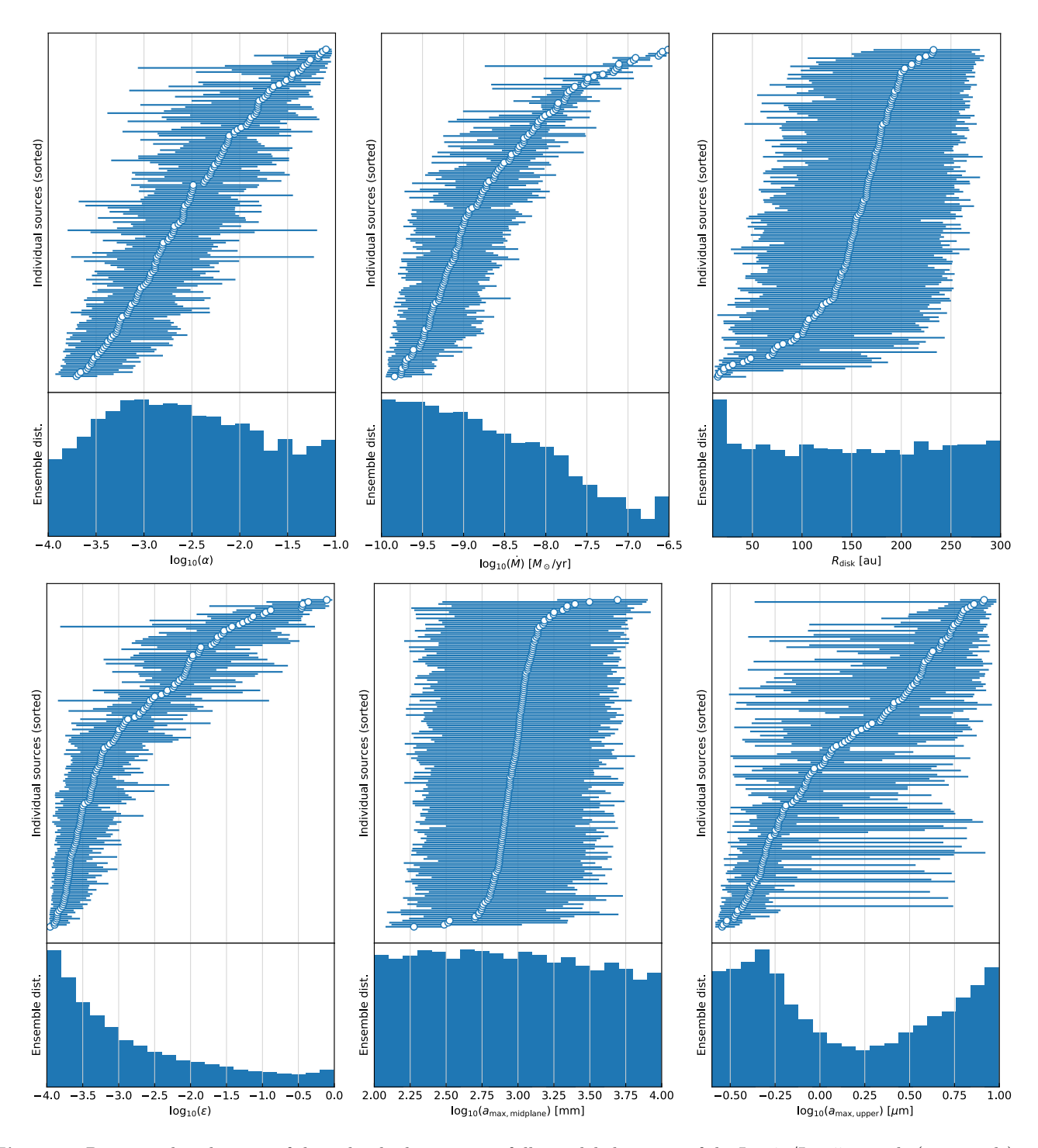


Figure 4. Posterior distributions of the individual 160 successfully modeled sources of the L1641/L1647 sample (top panels) and ensemble distribution (bottom panels) for the following parameters (from top left to bottom right):  $\alpha$  (disk viscosity),  $\dot{M}$  (mass accretion rate),  $R_{disk}$  (outer disk radius),  $\epsilon$  (dust settling),  $a_{max,midplane}$  (maximum grain size in the midplane),  $a_{max,upper}$  (maximum grain size in the upper layers of the disk). The error bars denote the 16th and 84th percentiles; the bottom panels' histograms use 20 bins.

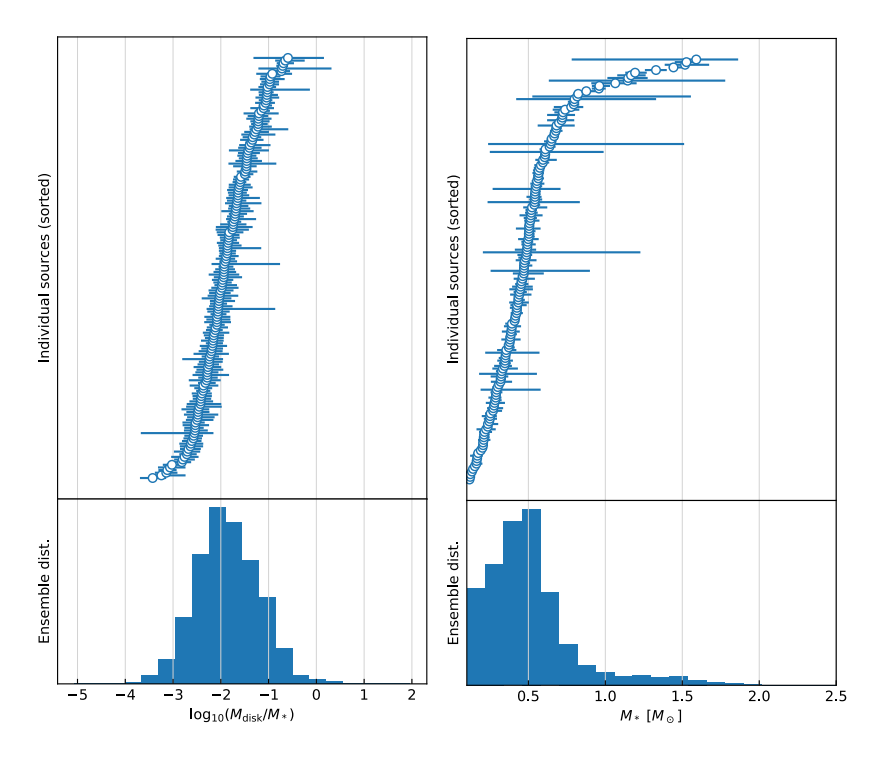


Figure 4. (Continued). Posterior distributions of the individual 160 successfully modeled sources of the L1641/L1647 sample (top panels) and ensemble distribution (bottom panels) for the following parameters (from left to right):  $M_{disk}/M_*$  (disk mass fraction to host star mass),  $M_*$  (host star mass).

Table 5. Posteriors for L1641/L1647 stellar and disk parameters

Object	$T_{eff}$	Radius	Mass	Parallax	$log_{10}(\dot{M})$
2MASS	K	$R_{\odot}$	$M_{\odot}$	mas	$M_{\odot}/yr$
J05334160-0606074	$3360^{+90}_{-90}$	$0.96^{+0.10}_{-0.10}$	$0.29^{+0.06}_{-0.06}$	$2.43^{+0.15}_{-0.14}$	$-8.9^{+0.4}_{-0.6}$
$\rm J05340108\text{-}0602268$	$3940^{+40}_{-40}$	$1.47^{+0.09}_{-0.09}$	$0.67^{+0.03}_{-0.03}$	$2.601^{+0.019}_{-0.018}$	$-8.12^{+0.11}_{-0.10}$
J05340495-0623469	$3440^{+50}_{-50}$	$1.22^{+0.11}_{-0.13}$	$0.33^{+0.04}_{-0.04}$	$2.61^{+0.05}_{-0.05}$	$-9.75^{+0.40}_{-0.19}$
J05342043-0631150	$3100^{+100}_{-100}$	$0.89^{+0.12}_{-0.12}$	$0.15^{+0.05}_{-0.04}$	$2.43^{+0.14}_{-0.15}$	$-9.7^{+0.4}_{-0.2}$
J05343360-0611194	$3020^{+50}_{-30}$	$1.04^{+0.08}_{-0.10}$	$0.122^{+0.014}_{-0.011}$	$2.58^{+0.07}_{-0.07}$	$-9.3^{+0.7}_{-0.4}$

$log_{10}(lpha)$	$log_{10}(\epsilon)$	$R_{disk}$ au	$\mathbf{a}_{ ext{max, upper}}$ $\mu ext{m}$	$a_{\max, \ midplane}$	$T_{wall}$ K	Inclination deg	$M_{dust}$ $M_{\oplus}$
$-2.4_{-0.7}^{+0.5}$ $-1.14_{-0.18}^{+0.10}$ $-2.5_{-0.5}^{+1.0}$ $-3.1_{-0.3}^{+0.4}$ $-2.6_{-0.5}^{+0.6}$	$-1.7^{+0.9}_{-0.8}$ $-3.7^{+0.3}_{-0.2}$ $-3.7^{+0.5}_{-0.2}$ $-3.7^{+0.5}_{-0.3}$ $-3.2^{+0.7}_{-0.5}$	$140^{+110}_{-100} \\ 60^{+120}_{-42} \\ 160^{+90}_{-90} \\ 170^{+90}_{-100} \\ 160^{+100}_{-100}$	$2.7_{-2.4}^{+5.0}$ $3.9_{-2.4}^{+4.0}$ $2.1_{-1.7}^{+5.0}$ $3.2_{-2.7}^{+4.0}$ $0.7_{-0.4}^{+4.0}$	$1100^{+4000}_{-900} \\ 800^{+4300}_{-700} \\ 1000^{+3000}_{-600} \\ 1000^{+3000}_{-700} \\ 1000^{+3000}_{-800}$	$1390^{+50}_{-50}$ $1440^{+40}_{-40}$ $1420^{+50}_{-50}$ $1420^{+50}_{-50}$ $1400^{+50}_{-40}$	$50^{+10}_{-23}$ $10^{+10}_{-5}$ $65^{+3}_{-12}$ $57^{+10}_{-20}$ $10^{+30}_{-9}$	$8^{+6}_{-3}$ $2^{+2}_{-1}$ $3^{+5}_{-2}$ $9^{+11}_{-5}$ $5^{+4}_{-2}$

NOTE—This table is published in its entirety in the machine-readable format. A portion is shown here for guidance regarding its form and content.

**Table 6.** Recalculated literature dust masses for the Serpens sample.

Object	$M_{dust}$
2MASS	$M_{\oplus}$
J18264598-0344306	$61 \pm 12$
$\rm J18264973\text{-}0355596$	$66 \pm 9$
J18274426-0329519	$90 \pm 12$
J18274445-0356016	$10.8\pm1.3$
J18275383-0002335	$6.3\pm1.4$
J18281519-0001408	$22 \pm 4$
J18290088+0029312	$100\pm10$
J18291969 + 0018030	$27 \pm 6$
J18293084 + 0101071	$4.1\pm1.7$
J18294147 + 0107378	$50 \pm 6$
J18295360 + 0117017	$14\pm4$
J18295820 + 0115216	$130\pm20$
J18300545 + 0101022	$10.3\pm2.9$
J18300610 + 0106170	$20 \pm 3$
J18302240+0120439	$17 \pm 3$
J18314416-0216182	$9.3 \pm 2.2$
J18321676-0223167	$15.9 \pm 2.9$
J18321707-0229531	$13\pm4$

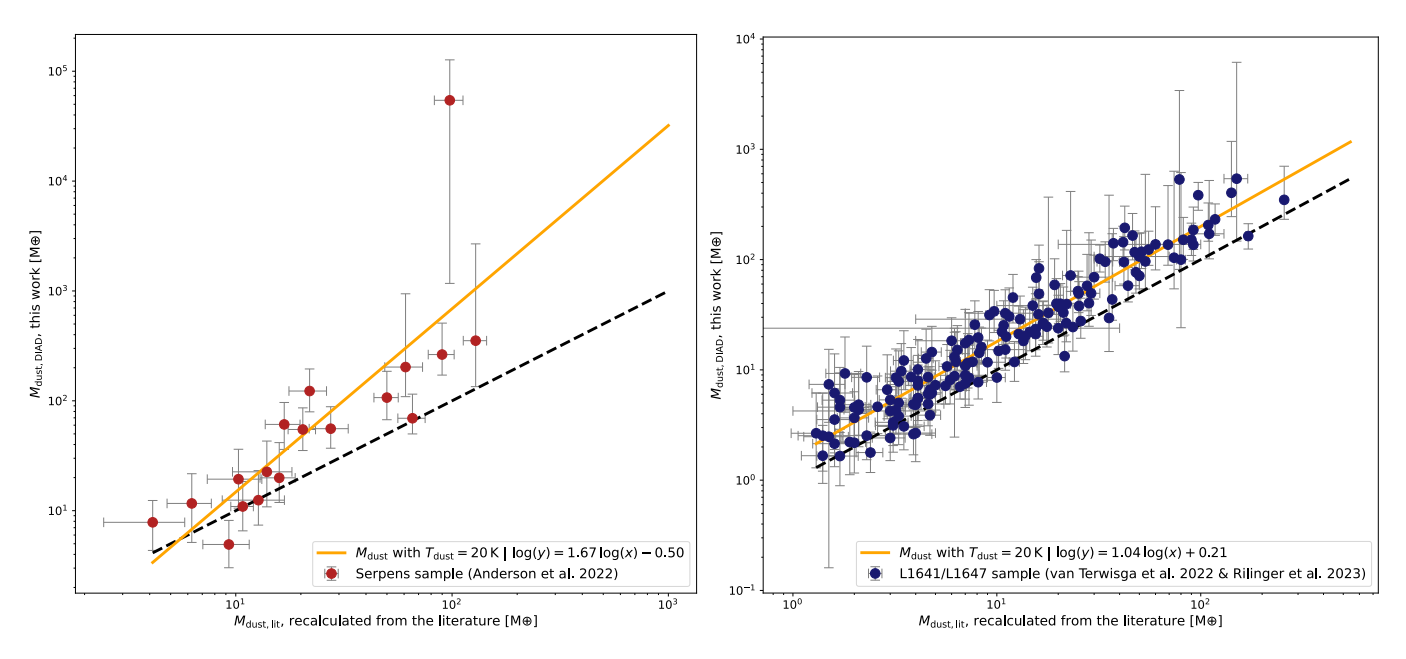


Figure 5. Comparison of this work's disk dust masses calculated from SED modeling and disk dust masses derived from millimeter fluxes from the literature; left panel corresponds to the Serpens sample (Anderson et al. 2022), right panel corresponds to the L1641/L1647 sample (van Terwisga et al. 2022; Rilinger et al. 2023). Both panels show a 1-to-1 relation (dotted black line) and a linear fit (solid orange line) that assumes a constant dust temperature of 20 K. The corresponding equation is noted for each linear fit.

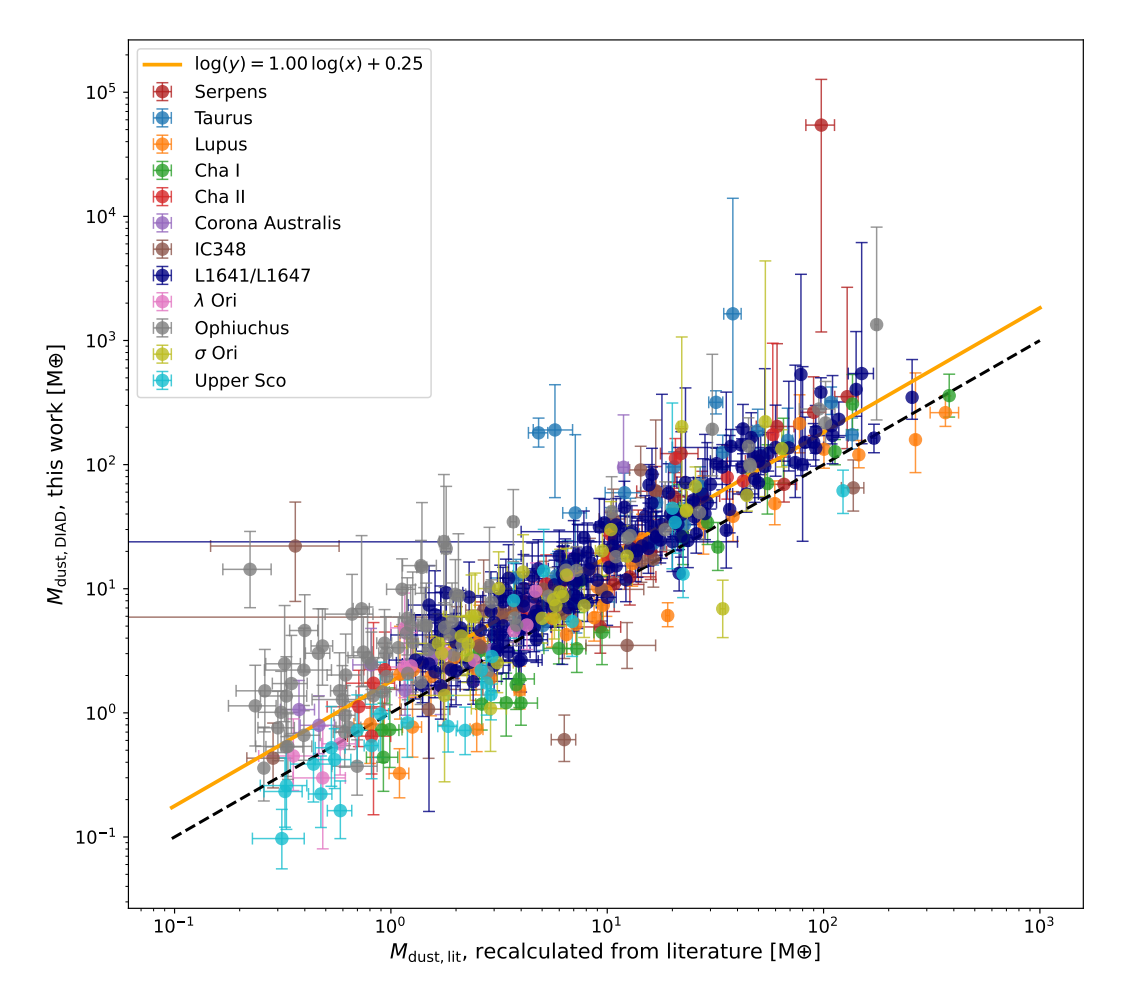


Figure 6. Comparison of this work's  $M_{dust}$  calculated from SED modeling and  $M_{dust}$  derived from millimeter fluxes from the literature; Serpens (Anderson et al. 2022) and L1641/L1647 (van Terwisga et al. 2022) data corresponds to this work, while data for the remaining 10 star-forming regions is gathered from Rilinger et al. (2023), where the same methodology was applied to calculate the masses. The solid orange line displays the linear fit to the recalculated dust masses, assuming a constant dust temperature of 20 K. The black dashed line denotes a 1-to-1 relation.

**Table 7.** Recalculated literature dust masses for L1641/L1647.

Object	$M_{dust}$
2MASS	$M_{\oplus}$
J05334160-0606074	$4.1 \pm 0.4$
J05340108-0602268	$1.9 \pm 0.4$
J05340495-0623469	$1.5\pm0.4$
J05341574-0636046	$42.0\pm2.0$
J05342043-0631150	$1.8\pm0.4$
J05343360-0611194	$2.0\pm0.4$
J05343614-0605346	$25.2 \pm 0.4$
J05344765-0619401	$7.6 \pm 0.3$
J05344833-0630268	$20.1 \pm 0.4$
J05345404-0623507	$82.1 \pm 0.4$

<sup>\*</sup>This table is published in its entirety in the machine-readable format. A portion is shown here for guidance regarding its form and content.

that these regions have different sample sizes, so it is likely that these values are influenced by the number of objects.

The explanation that has been proposed for the discrepancy in disk masses seen above is that Equation 1 assumes that the disk emission is optically thin at the reference frequency, and this may not be true in all cases. For example, there are cases where the spectral index of the inner regions drops below 2 (i.e., TW Hya (Huang et al. 2018; Macías et al. 2021), Elias 2-27 (Paneque-Carreño et al. 2021), and MP Mus (Ribas et al. 2023)), indicating that the emission is optically thick. If the disk is optically thick at certain wavelengths, the observed flux will not be sensitive to the total dust mass of the disk, and so Equation 1 will underestimate  $M_d$ .

We demonstrate that our larger dust mass estimates – when compared with flux-based dust mass estimates – are mostly driven by high optical depths at (sub-)mm wavelengths in Figure 7. Following the same methodology detailed in Xin et al. (2023), we used the median values obtained from the ANN as input parameters to generate DIAD models from which we calculate the structure of the disk and the optical depth along the line of sight as a function of the radius at 225 GHz (1.3 mm). This is followed by computing a flux-weighted mean optical depth where the flux at each radius is used as the weight for the optical depth corresponding to that radius. These weights are calculated based on the inten-

sity, disk radius, and inclination angle, which are further computed by considering the area difference between adjacent radii and the flux at each point, accounting for the inclination angle. The single average optical depth results from the mean of the optical depths weighted by the flux-derived weights. Panels (a) and (b) display the flux-weighted mean optical depths versus disk dust masses and disk sizes (respectively) for the samples of Taurus, Serpens, Lupus, Cha I, and Upper Sco, while for L1641/L1647, we include 10% of the sample to avoid overpopulating the plots. The marker size indicates disk radius (in au), and the black broken line denotes  $\tau_{\omega} = 1$ . Panel (a) shows that as we move toward greater disk dust masses, the mean optical depth tends to increase. Panel (b) shows that a similar trend of increasing mean optical depths occurs for smaller disk sizes, since the disk total mass gets concentrated in a smaller area, hence increasing the optical depth. Panel (c) displays again the mean optical depth, plotted against a disk dust mass ratio, i.e., the disk dust mass estimated from DIAD divided by the disk dust mass estimated from the (sub-)mm flux using Equation 1. In addition, panel (c) also shows the disk dust mass derived from DIAD in the color scale, and the disk size as shown by the marker size (like in panels (a) and (b)). Panel (c) clearly demonstrates that higher disk dust mass discrepancy factors are caused by high optical depths. The three panels together show that these high optical depths are mostly driven by high disk dust masses and small disk sizes. In other words, flux-based disk dust masses are underestimated to a greater extent for disks that are more massive and/or more compact. These results highlight the importance of properly accounting for the optical depth of the disk, as high optical depths at (sub-)mm wavelengths can cause underestimation of disk mass when relying solely on flux-based estimates assuming optically thin emission.

# 4.2. Comparison of Serpens & L1641/L1647 with other Star-Forming Regions

Here, we compare the results obtained for Serpens and L1641/L1647 with the 10 other star-forming regions studied in Rilinger et al. (2023). These regions span an

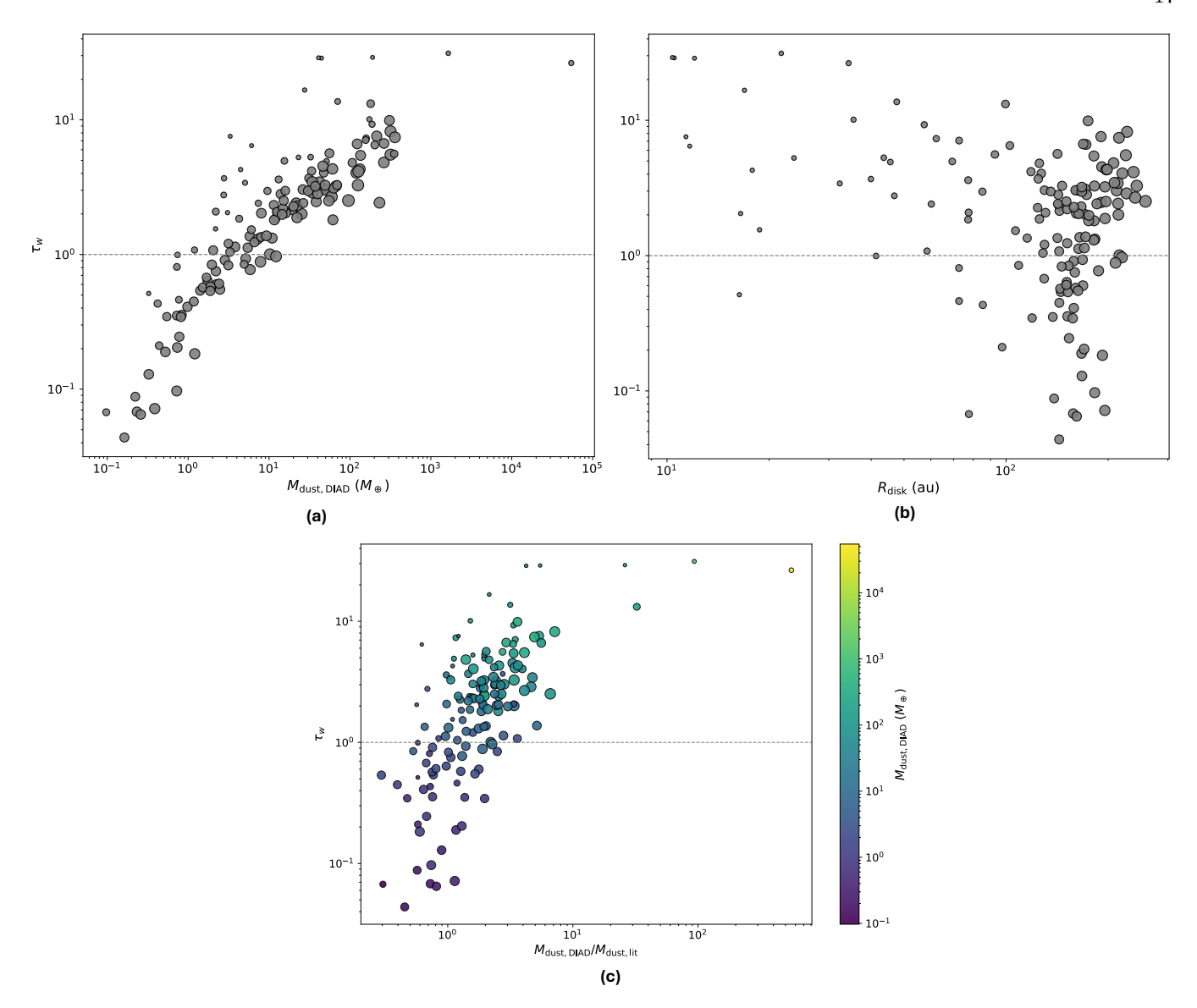


Figure 7. Comparison of flux-weighted mean optical depth for subsets of disks in different star-forming regions (i.e., L1641/L1647 [1.5 Myr], Taurus [1-2 Myr], Serpens [1-3 Myr], Lupus [1-3 Myr], Cha I [2-3 Myr], and Upper Sco [5-10 Myr]) plotted versus (a) disk dust mass, (b) disk size, and (c) disk dust mass ratio (i.e.,  $M_{dust,DIAD}/M_{dust,lit}$ ). Optical depths are obtained from flux-weighted averages of the 1.3 mm optical depth at each radius in the disk, calculated using the DIAD models. Optical depth values for the Lupus, Taurus, Cha I, and Upper Sco regions are adopted from Rilinger et al. (2023). The denoted disk masses correspond to the median value of the distribution obtained for each object. The color bar in panel (c) indicates the dust mass of the disk. In all three panels, marker size increases proportionally with the size of  $R_{disk}$ ) (in au), and the black broken line represents  $\tau_{\omega} = 1$ .

age range from  $\sim 0.5\text{-}10 \text{ Myr.}^1$  Figure 8 shows how the Serpens and L1641/L1647 dust mass distributions compare to the star-forming regions studied in Rilinger et al. (2023). The peak of the mass distribution tends to shift to lower masses for older regions. Regions such as Serpens, Taurus, and L1641/L1647 (i.e., < 3 Myr) have median dust masses above the overall median ( $\sim 9.28$  $M_{\oplus}$ ), while older regions such as Upper Sco and  $\lambda$  Ori (i.e., > 3 Myr) have dust masses that are below the overall median. Figure 9 is also consistent with the finding that disk dust mass generally decreases with age (e.g., Ansdell et al. 2016; Barenfeld et al. 2016; Pascucci et al. 2016; Cieza et al. 2019; van Terwisga et al. 2019; Villenave et al. 2021; van Terwisga et al. 2022; Rilinger et al. 2023). We note that the objects included in each region are biased towards higher masses as we only include sources with millimeter-wavelength detections. Additionally, each survey adopts a different detection limit (van Terwisga et al. 2022; Anderson et al. 2022; Rilinger et al. 2023).

# 4.3. The "missing mass" problem

One possible solution to the "missing mass" problem is that disk dust masses are underestimated. In this work, as in other works (Ballering & Eisner 2019; Ribas et al. 2020; Xin et al. 2023; Rilinger et al. 2023), we find that disk dust masses can be underestimated when using millimeter fluxes alone. To further explore whether this can solve the "missing mass" problem, we compare observed exoplanet systems and the available dust mass in protoplanetary disks.

Figure 10 compares the cumulative distribution function (CDF) for the dust mass content in Serpens and L1641/L1647 from this work (i.e., SED model derived; red line and blue line, respectively), the dust mass content using Anderson et al. (2022) & van Terwisga et al. (2022) millimeter fluxes (light red line and light blue line, respectively), and the mass content observed in currently known exoplanets (gray line). The masses of presently known and confirmed exoplanets were gath-

ered from the NASA Exoplanet Archive, amounting to a sample of 3401 exoplanets with known masses and respective errors. The black cumulative distribution function denotes the masses of exoplanet systems, which are normalized to the observed fraction of gaseous planets (Cumming et al. 2008). Based on observations, gaseous planets are rarer than rocky low-mass planets. As shown in Mayor et al. (2011), about 50% of solar-type stars host planets with a mass upper limit  $< 30 M_{\oplus}$ . Cumming et al. (2008) estimates that about 17%-19% of stars host gas giants within 20 au. Following the methodology detailed in Tychoniec et al. (2020), we restrict our sample to only systems containing at least one planet with a total mass  $> 0.3 M_{Jup}$ , as detectability increases for objects with periods as large as 2000 days (Cumming et al. 2008). We normalize these systems by setting the 18% value of the CDF at the estimated solid fraction of the gaseous planet of 0.3  $M_{Jup}$  (i.e., 27.8  $M_{\oplus}$ ). Thus, we limit our sample to only those objects that are detectable and have a known solid material content (were the solid mass for gaseous planets is estimated using the formula from Thorngren et al. 2016). Figure 10 shows how, despite accounting for disk mass underestimation, the "missing mass" issue persists, implying that the problem is more complicated and may involve multiple factors.

As mentioned in Section 1, the "lack" of mass can also be explained by earlier planet formation (i.e., happening as early as the Class 0 and Class I stages), as discussed in Tychoniec et al. (2020) where they compare Class 0, Class I, and Class II objects from the Perseus and Orion star-forming regions. In both instances, the CDF for Class II objects does not follow the CDF for exoplanets at greater masses. If planet formation occurs earlier (i.e., during the Class O and/or Class I stages), then the dust masses we are measuring for Class II objects may only represent that of the remnant material of planet formation.

It is also possible that we are still underestimating the dust masses. First, we are not sensitive to grains > 1 mm. In addition, there may be significant dust in optically thick disk substructures (Savvidou & Bitsch 2024). To more accurately measure disk dust masses, observations at longer wavelengths are necessary. Xin et al. (2023) showed that disks become optically thinner at 3 mm relative to 1.3 mm. In Figure 11, we calculate the optical depth at a longer reference wavelength of 7mm corresponding to ALMA band 1 for Serpens and L1641/L1647. We find that the vast majority of objects become optically thin at 7 mm. Thus, observations at longer mm wavelengths (i.e., ALMA band 3 and band

<sup>&</sup>lt;sup>1</sup> We remove the following eight objects from the Lupus sample adopted in Rilinger et al. (2023) due to their uncertain membership: 2MASS J15450634-3417378 and 2MASS J16075475-3915446 are not detected in Gaia DR3; 2MASS J16070384-3911113 is detected in Gaia DR3 but has no parallax measurement; 2MASS J15560210-3655282, 2MASS J16030548-4018254, and 2MASS J16124373-3815031 have kinematics consistent with Lupus, but also Sco-Cen Luhman (2020), making their membership unlikely; 2MASS J15592523-4235066 has kinematics inconsistent with Lupus and instead indicative of Upper Centaurus-Lupus and Lower Centaurus-Crux; and Sz 90, which has Gaia DR2 astrometry that supports membership in Lupus, but Gaia DR3 data does not support it.

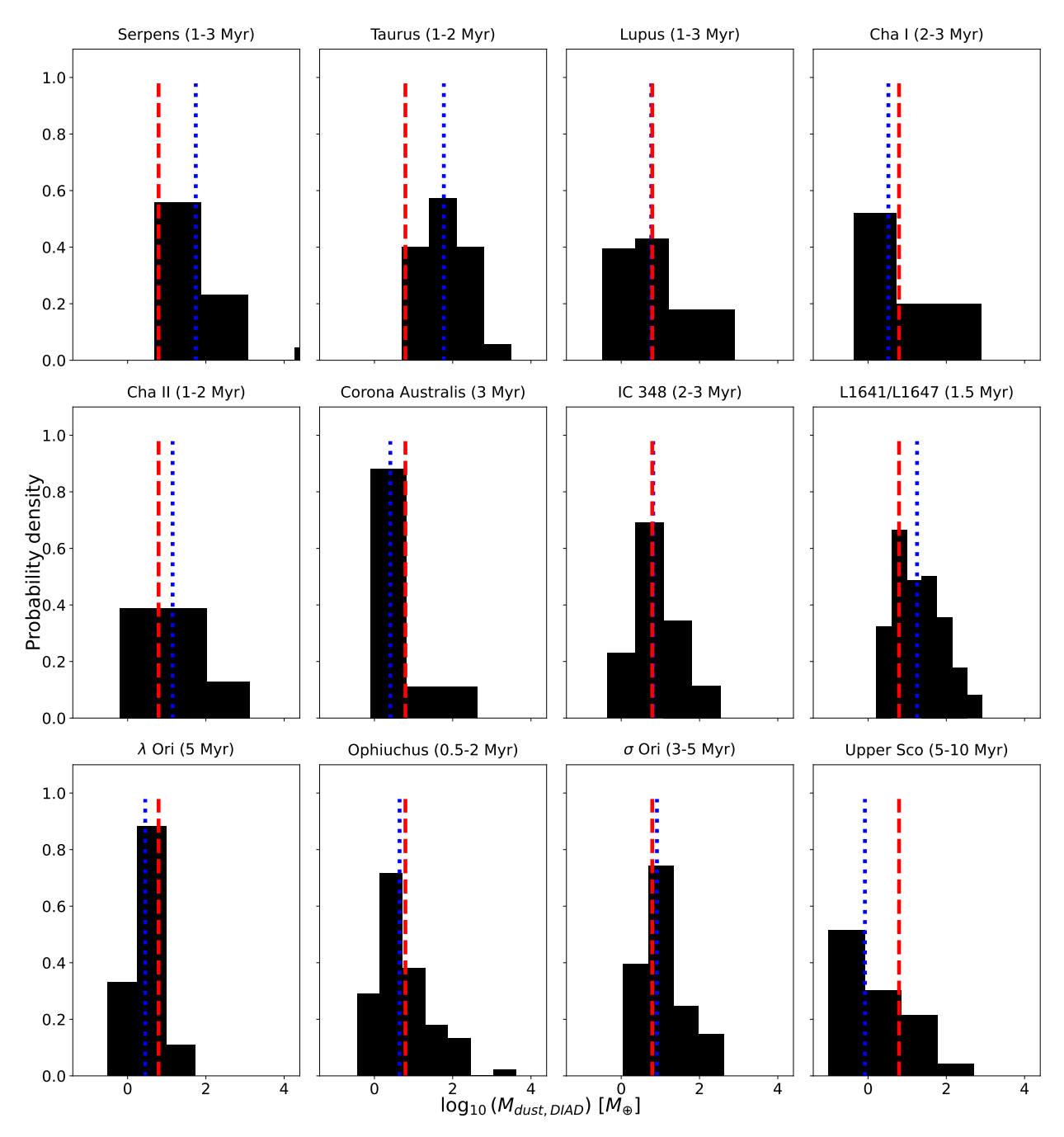


Figure 8. Probability density functions of  $M_{dust}$  for 12 star forming regions. Blue dashed lines denote the median for each region, and red dotted lines denote the median for all regions ( $\sim$ 9.28  $M_{\oplus}$ ). Serpens and L1641/L1647 data correspond to this work, while data for the remaining star-forming regions is gathered from Rilinger et al. (2023).

1) are essential to better characterize the dust content of disks.

#### 5. SUMMARY

We calculated disk dust masses for a sample of 178 TTS, 18 located in the Serpens star-forming region and 160 in the L1641 & L1647 regions, using multi-wavelength photometry and *Spitzer* IRS spectra (when available) and an ANN trained with DIAD models (fol-

lowing Ribas et al. (2020)). The sample was obtained from ALMA 1.3 mm continuum band surveys of Serpens (Anderson et al. 2022) and the L1641 & L1647 regions of the Orion A cloud (van Terwisga et al. 2022). Our work measured disk dust masses using SED modeling and the key findings are as follows:

• Disk dust masses calculated from SED modeling are, on average, a factor of 2.0 times higher for

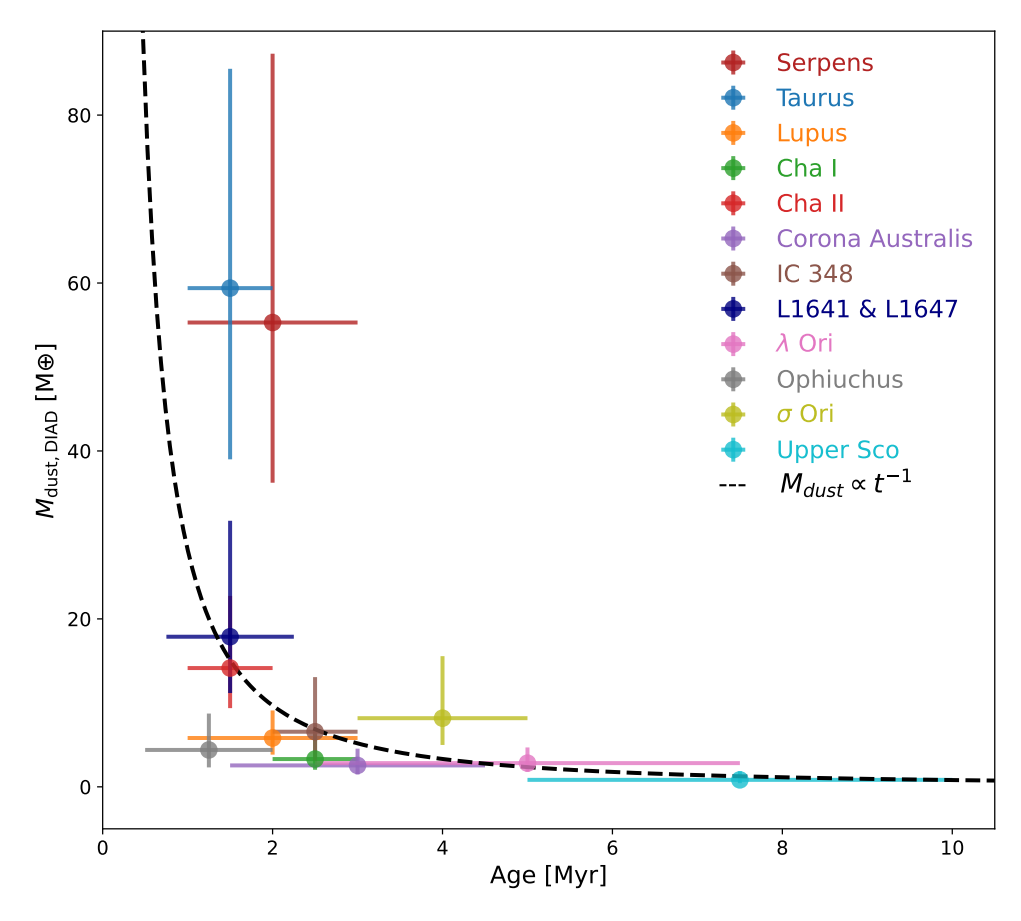


Figure 9. Median dust masses for 12 star-forming regions compared to the respective age of each region. Following Rilinger et al. (2023), the black dashed line denotes the dust depletion function  $M_{dust} \propto t^{-1}$  (Testi et al. 2022), and scales it by the weighted mean mass at 1.5 Myr. Median values for  $M_{dust}$  are calculated for each region. Serpens data correspond to this work, while data for the remaining star-forming regions is gathered from Rilinger et al. (2023).

both Serpens and L1641/L1647 than those computed using mm-fluxes at 1.3mm. This is consistent with previous work done in other regions by Ribas et al. (2020); Xin et al. (2023); Rilinger et al. (2023), where a similar methodology was followed. We conclude that this is because most disk dust masses calculated using mm-fluxes assume that the disk is optically thin, whereas we find that many disks are still optically thick at 1.3mm.

• When compared to 10 other star-forming regions that range from  $\sim 0.5$  to  $\sim 10$  Myr (Rilinger et al. 2023), Serpens and L1641/L1647 follow the tendency of younger regions (e.g., Taurus, Cha II,  $\sigma$  Ori) to display a greater median disk dust mass than the overall average. Serpens' median disk dust mass is  $\sim 55.3~M_{\oplus}$ , and L1641/L1647's median disk dust mass is  $\sim 17.9~M_{\oplus}$ ; whereas the median for all 12 star-forming regions is  $\sim 9.28~M_{\oplus}$ .

- Dust masses for Serpens and L1641/L1647 follow the observed relation between dust mass and age (i.e.,  $M_{dust} \propto t^{-1}$ ).
- We calculated the optical depths of a subset of disks in Serpens and L1641/L1647 at 1.3mm and 7mm and found that most disks are optically thick at 1.3mm while the vast majority are optically thin at 7 mm.

Future ALMA surveys are needed at longer wavelengths where the disk is more likely to be optically thin (e.g., band 1) to more accurately measure disk dust masses. This will allow for a more detailed view of disk evolution and planet formation as well as comparison with exoplanet populations.

# ACKNOWLEDGMENTS

This work was funded by NASA ADAP 80NSSC20K0451. Álvaro Ribas has been supported by the UK Science and Technology Facilities Council (STFC) via the consolidated grant ST/W000997/1 and

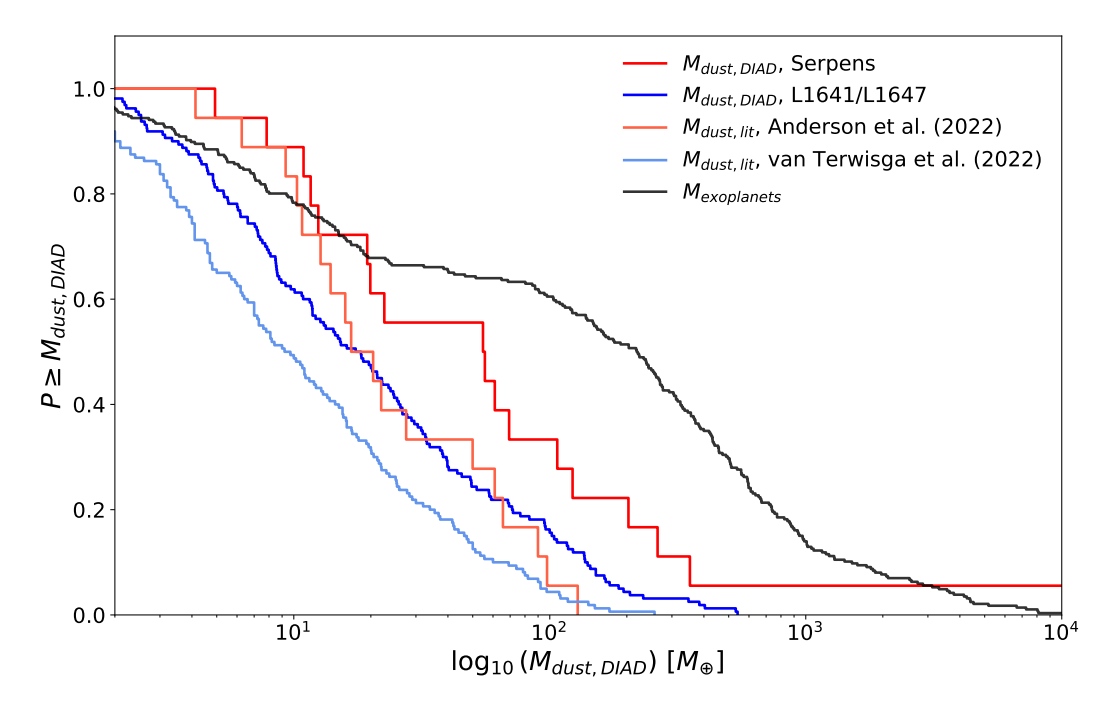


Figure 10. Comparison of cumulative distribution functions which correspond to dust masses of Serpens (red line) and L1641/L1647 (blue line) gathered from this work, and Serpens' (light red line) and L1641/L1647's (light blue line) dust masses recalculated using literature millimeter fluxes (Anderson et al. 2022; van Terwisga et al. 2022) in Equation 1, and mass content available in confirmed exoplanets which are above the detectability threshold (i.e.,  $> 0.3 M_{Jup}$ ), using data gathered from the NASA Exoplanet Archive (black line). The cumulative distribution functions were developed using the Kaplan-Meier fitting method.

by the European Union's Horizon 2020 research and innovation programme under the Marie Sklodowska-Curie grant agreement No. 823823 (RISE DUST-BUSTERS project). We thank Alexa R. Anderson, Jesús Hernández, Kevin Luhman, Anneliese M. Rilinger, and Zihua Xin for insightful discussions. This paper utilizes the D'Alessio Irradiated Accretion Disk (DIAD) code. We acknowledge the important work carried out by Paola D'Alessio, who passed away in 2013. Without her, works like these could not have been achieved.

This paper makes use of the following ALMA data: ADS/JAO.ALMA#2019.1.00218.S and ADS/JAO.ALMA#2019.1.01813.S. ALMA is a partnership of ESO (representing its member states), NSF (USA) and NINS (Japan), together with NRC (Canada), NSTC and ASIAA (Taiwan), and KASI (Republic of Korea), in cooperation with the Republic of Chile. The Joint ALMA Observatory is operated by ESO, AUI/NRAO and NAOJ. The National Radio Astronomy Observatory is a facility of the National Science Foundation operated under cooperative agreement by Associated Universities, Inc.

This research has made use of the NASA Exoplanet Archive, which is operated by the California Institute of Technology, under contract with the National Aeronautics and Space Administration under the Exoplanet Exploration Program. This work has made use of the interactive graphical viewer and editor for tabular data TOPCAT (Taylor 2005). This research has made use of the VizieR catalogue access tool, CDS, Strasbourg, France (DOI: 10.26093/cds/vizier). The original description of the VizieR service was published in Ochsenbein et al. (2000). This research has made use of the SIMBAD database (Wenger et al. 2000), operated at CDS, Strasbourg, France. This work has made use of data from the European Space Agency (ESA) mission Gaia, processed by the Gaia Data Processing and Analysis Consortium (DPAC).

Software: Astropy (Astropy Collaboration et al. 2013, 2018, 2022), NumPy (Harris et al. 2020), SciPy (Virtanen et al. 2020), lifelines (Davidson-Pilon 2022), matplotlib (Hunter 2007), pandas (Reback et al. 2022)

# REFERENCES

Abdurro'Uf, & et al. 2023, VizieR Online Data Catalog: APOGEE-2 DR17 final allStar catalog (Abdurro'uf+, 2022), VizieR On-line Data Catalog: III/286. Originally published in: 2022ApJS..259...35A Ahumada, R., Allende Prieto, C., Almeida, A., et al. 2020, ApJS, 249, 3, doi: 10.3847/1538-4365/ab929e

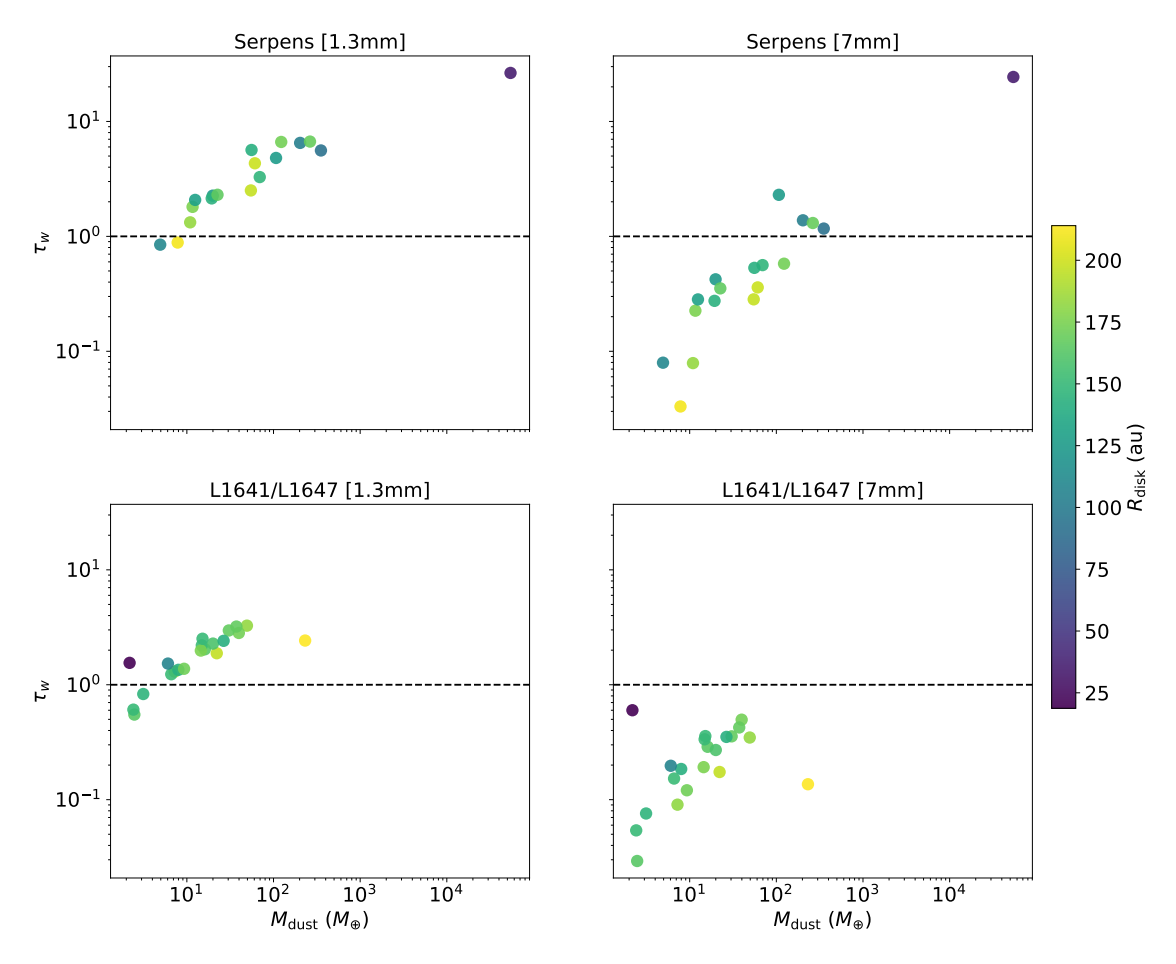


Figure 11. Comparison of flux-weighted mean optical depth for a subset of disks in Serpens (top) and L1641/L1647 (bottom) plotted versus disk dust mass. Optical depths are gathered from flux-weighted averages of the 1.3 mm (left) and 7 mm (right) optical depth at each radius in the disk, calculated using the DIAD models. Denoted disk masses correspond to the median value of the distribution obtained for each object. We note that for Serpens we show the whole sample of 18 objects, while for L1641/L1647 we show the 10% of the sample. The color bar denotes the disk's outer radius (in au). The black broken line represents  $\tau_{\omega} = 1$ .

Akeson, R. L., Jensen, E. L. N., Carpenter, J., et al. 2019, ApJ, 872, 158, doi: 10.3847/1538-4357/aaff6a

ALMA Partnership, Brogan, C. L., Pérez, L. M., et al. 2015, ApJL, 808, L3, doi: 10.1088/2041-8205/808/1/L3

Anderson, A. R., Williams, J. P., van der Marel, N., et al. 2022, ApJ, 938, 55, doi: 10.3847/1538-4357/ac8ff0

Andrae, R., Fouesneau, M., Creevey, O., et al. 2018, A&A, 616, A8, doi: 10.1051/0004-6361/201732516

Andrae, R., Fouesneau, M., Sordo, R., et al. 2023, A&A, 674, A27, doi: 10.1051/0004-6361/202243462

Andrews, S. M., Rosenfeld, K. A., Kraus, A. L., & Wilner, D. J. 2013, ApJ, 771, 129,

doi: 10.1088/0004-637X/771/2/129

Andrews, S. M., & Williams, J. P. 2005, ApJ, 631, 1134, doi: 10.1086/432712 Andrews, S. M., Wilner, D. J., Macías, E.,

Carrasco-González, C., & Isella, A. 2018, in Astronomical Society of the Pacific Conference Series, Vol. 517, Science with a Next Generation Very Large Array, ed.

E. Murphy, 137

Ansdell, M., Williams, J. P., Manara, C. F., et al. 2017, AJ, 153, 240, doi: 10.3847/1538-3881/aa69c0

Ansdell, M., Williams, J. P., van der Marel, N., et al. 2016, ApJ, 828, 46, doi: 10.3847/0004-637X/828/1/46

Artymowicz, P., & Lubow, S. H. 1994, ApJ, 421, 651, doi: 10.1086/173679

Astropy Collaboration, Robitaille, T. P., Tollerud, E. J., et al. 2013, A&A, 558, A33, doi: 10.1051/0004-6361/201322068

Astropy Collaboration, Price-Whelan, A. M., Sipőcz, B. M., et al. 2018, AJ, 156, 123, doi: 10.3847/1538-3881/aabc4f Astropy Collaboration, Price-Whelan, A. M., Lim, P. L., et al. 2022, ApJ, 935, 167, doi: 10.3847/1538-4357/ac7c74

- Bailer-Jones, C. A. L., Andrae, R., Arcay, B., et al. 2013, A&A, 559, A74, doi: 10.1051/0004-6361/201322344
- Ballering, N. P., & Eisner, J. A. 2019, AJ, 157, 144, doi: 10.3847/1538-3881/ab0a56
- Barenfeld, S. A., Carpenter, J. M., Ricci, L., & Isella, A. 2016, ApJ, 827, 142, doi: 10.3847/0004-637X/827/2/142
- Barenfeld, S. A., Carpenter, J. M., Sargent, A. I., et al. 2019, ApJ, 878, 45, doi: 10.3847/1538-4357/ab1e50
- Beckwith, S. V. W., Sargent, A. I., Chini, R. S., & Guesten, R. 1990, AJ, 99, 924, doi: 10.1086/115385
- Bergin, E. A., & Williams, J. P. 2018, arXiv e-prints, arXiv:1807.09631, doi: 10.48550/arXiv.1807.09631
- Birnstiel, T., Dullemond, C. P., & Brauer, F. 2010, A&A, 513, A79, doi: 10.1051/0004-6361/200913731
- Cacciapuoti, L., Testi, L., Podio, L., et al. 2024, The
   Astrophysical Journal, 961, 90,
   doi: 10.3847/1538-4357/ad0f17
- Cazzoletti, P., Manara, C. F., Liu, H. B., et al. 2019, A&A, 626, A11, doi: 10.1051/0004-6361/201935273
- Chambers, K. C., Magnier, E. A., Metcalfe, N., et al. 2016, arXiv e-prints, arXiv:1612.05560, doi: 10.48550/arXiv.1612.05560
- Choi, J., Dotter, A., Conroy, C., et al. 2016, ApJ, 823, 102, doi: 10.3847/0004-637X/823/2/102
- Cieza, L. A., Padgett, D. L., Allen, L. E., et al. 2009, ApJL, 696, L84, doi: 10.1088/0004-637X/696/1/L84
- Cieza, L. A., Ruíz-Rodríguez, D., Hales, A., et al. 2019, MNRAS, 482, 698, doi: 10.1093/mnras/sty2653
- Cox, E. G., Harris, R. J., Looney, L. W., et al. 2017, ApJ, 851, 83, doi: 10.3847/1538-4357/aa97e2
- Cumming, A., Butler, R. P., Marcy, G. W., et al. 2008, PASP, 120, 531, doi: 10.1086/588487
- Cutri, R. M., Wright, E. L., Conrow, T., et al. 2021, VizieR Online Data Catalog, II/328
- da Rio, N., Tan, J. C., Covey, K. R., et al. 2016, VizieR
  Online Data Catalog: IN-SYNC. IV. YSOs in Orion A
  (Da Rio+, 2016), VizieR On-line Data Catalog:
  J/ApJ/818/59. Originally published in:
  2016ApJ...818...59D, doi: 10.26093/cds/vizier.18180059
- D'Alessio, P., Calvet, N., & Hartmann, L. 2001, ApJ, 553, 321, doi: 10.1086/320655
- D'Alessio, P., Calvet, N., Hartmann, L., Franco-Hernández, R., & Servín, H. 2006, ApJ, 638, 314, doi: 10.1086/498861
- D'Alessio, P., Calvet, N., Hartmann, L., Lizano, S., & Cantó, J. 1999, ApJ, 527, 893, doi: 10.1086/308103
- D'Alessio, P., Cantö, J., Calvet, N., & Lizano, S. 1998, ApJ, 500, 411, doi: 10.1086/305702
- D'Alessio, P., Hartmann, L., Calvet, N., et al. 2005, ApJ, 621, 461, doi: 10.1086/427490

- Davidson-Pilon, C. 2022, lifelines, survival analysis in Python, v0.27.4, Zenodo, doi: 10.5281/zenodo.7329096
  Dotter, A. 2016, ApJS, 222, 8, doi: 10.3847/0067-0049/222/1/8
- Dunham, M. M., Allen, L. E., Evans, Neal J., I., et al. 2015, ApJS, 220, 11, doi: 10.1088/0067-0049/220/1/11
- Erickson, K. L., Wilking, B. A., Meyer, M. R., et al. 2015, AJ, 149, 103, doi: 10.1088/0004-6256/149/3/103
- Evans, Neal J., I., Allen, L. E., Blake, G. A., et al. 2003, PASP, 115, 965, doi: 10.1086/376697
- Evans, N. J., Dunham, M. M., Jorgensen, J. K., et al. 2009, VizieR Online Data Catalog, J/ApJS/181/321, doi: 10.26093/cds/vizier.21810321
- Fang, M., Kim, J. S., van Boekel, R., et al. 2013, ApJS, 207, 5, doi: 10.1088/0067-0049/207/1/5
- Fang, M., van Boekel, R., Wang, W., et al. 2009, A&A, 504, 461, doi: 10.1051/0004-6361/200912468
- Fang, M., Kim, J. S., Pascucci, I., et al. 2018, VizieR Online Data Catalog: Spectroscopy of the foreground population in Orion A (Fang+, 2017), VizieR On-line Data Catalog: J/AJ/153/188. Originally published in: 2017AJ....153..188F, doi: 10.26093/cds/vizier.51530188
- Foreman-Mackey, D., Hogg, D. W., Lang, D., & Goodman, J. 2013, PASP, 125, 306, doi: 10.1086/670067
- Gaia Collaboration, Brown, A. G. A., Vallenari, A., et al. 2018, A&A, 616, A1, doi: 10.1051/0004-6361/201833051
- Gaia Collaboration, Vallenari, A., Brown, A. G. A., et al. 2023, A&A, 674, A1, doi: 10.1051/0004-6361/202243940
- Ginski, C., Facchini, S., Huang, J., et al. 2021, ApJL, 908, L25, doi: 10.3847/2041-8213/abdf57
- Goodman, A. A., Benson, P. J., Fuller, G. A., & Myers, P. C. 1993, ApJ, 406, 528, doi: 10.1086/172465
- Grant, S. L., Espaillat, C. C., Megeath, S. T., et al. 2018, ApJ, 863, 13, doi: 10.3847/1538-4357/aacda7
- Grant, S. L., Espaillat, C. C., Wendeborn, J., et al. 2021, ApJ, 913, 123, doi: 10.3847/1538-4357/abf432
- Großschedl, J. E., Alves, J., Teixeira, P. S., et al. 2019, A&A, 622, A149, doi: 10.1051/0004-6361/201832577
- Guzmán-Díaz, J., Mendigutía, I., Montesinos, B., et al. 2021, A&A, 650, A182, doi: 10.1051/0004-6361/202039519
- Harris, C. R., Millman, K. J., van der Walt, S. J., et al. 2020, Nature, 585, 357, doi: 10.1038/s41586-020-2649-2
- Harris, R. J., Andrews, S. M., Wilner, D. J., & Kraus, A. L. 2012, ApJ, 751, 115, doi: 10.1088/0004-637X/751/2/115
- Harvey, P., Merín, B., Huard, T. L., et al. 2007, ApJ, 663, 1149, doi: 10.1086/518646
- Henden, A. A., Templeton, M., Terrell, D., et al. 2016, VizieR Online Data Catalog, II/336

- Herbig, G. H. 1962, Advances in Astronomy and Astrophysics, 1, 47,
  - doi: 10.1016/B978-1-4831-9919-1.50006-6
- Hernández, J., Zamudio, L. F., Briceño, C., et al. 2023, AJ, 165, 205, doi: 10.3847/1538-3881/acc467
- Hildebrand, R. H. 1983, QJRAS, 24, 267
- Hogg, D. W., Bovy, J., & Lang, D. 2010, arXiv e-prints, arXiv:1008.4686, doi: 10.48550/arXiv.1008.4686
- Houck, J. R., Roellig, T. L., van Cleve, J., et al. 2004, ApJS, 154, 18, doi: 10.1086/423134
- Hsu, W.-H., Hartmann, L., Allen, L., et al. 2012, ApJ, 752, 59, doi: 10.1088/0004-637X/752/1/59
- —. 2013, ApJ, 764, 114, doi: 10.1088/0004-637X/764/2/114
- Huang, J., Andrews, S. M., Cleeves, L. I., et al. 2018, ApJ, 852, 122, doi: 10.3847/1538-4357/aaa1e7
- Hunter, J. D. 2007, Computing in Science and Engineering, 9, 90, doi: 10.1109/MCSE.2007.55
- Joy, A. H. 1945, ApJ, 102, 168, doi: 10.1086/144749
- Kim, K. H., Watson, D. M., Manoj, P., et al. 2013, ApJ, 769, 149, doi: 10.1088/0004-637X/769/2/149
- —. 2016, VizieR Online Data Catalog: Spitzer/IRS survey of Class II objects in Orion A. I. (Kim+, 2016), VizieR On-line Data Catalog: J/ApJS/226/8. Originally published in: 2016ApJS..226....8K, doi: 10.26093/cds/vizier.22260008
- Kounkel, M., Megeath, S. T., Poteet, C. A., Fischer, W. J., & Hartmann, L. 2016, VizieR Online Data Catalog: NIR survey of Spitzer YSOs in Orion Mol. Cloud (Kounkel+, 2016), VizieR On-line Data Catalog: J/ApJ/821/52. Originally published in: 2016ApJ...821...52K, doi: 10.26093/cds/vizier.18210052
- Kraus, A. L., Ireland, M. J., Hillenbrand, L. A., & Martinache, F. 2012, ApJ, 745, 19, doi: 10.1088/0004-637X/745/1/19
- Kuffmeier, M., Haugbølle, T., & Nordlund, Å. 2017, ApJ, 846, 7, doi: 10.3847/1538-4357/aa7c64
- Lasker, B. M., Lattanzi, M. G., McLean, B. J., et al. 2008, AJ, 136, 735, doi: 10.1088/0004-6256/136/2/735
- Lebouteiller, V., Barry, D. J., Spoon, H. W. W., et al. 2011, ApJS, 196, 8, doi: 10.1088/0067-0049/196/1/8
- Lindegren, L., Bastian, U., Biermann, M., et al. 2021, A&A, 649, A4, doi: 10.1051/0004-6361/202039653
- Liu, M., He, J., Ge, J., et al. 2023, ApJ, 943, 39, doi: 10.3847/1538-4357/aca658
- Liu, Y., Linz, H., Fang, M., et al. 2022, A&A, 668, A175, doi: 10.1051/0004-6361/202244505
- Luhman, K. L. 2020, AJ, 160, 186, doi: 10.3847/1538-3881/abb12f
- Luhman, K. L., & Esplin, T. L. 2020, AJ, 160, 44, doi: 10.3847/1538-3881/ab9599

- Macías, E., Guerra-Alvarado, O., Carrasco-González, C., et al. 2021, A&A, 648, A33, doi: 10.1051/0004-6361/202039812
- Manara, C. F., Morbidelli, A., & Guillot, T. 2018, A&A, 618, L3, doi: 10.1051/0004-6361/201834076
- Marton, G., Calzoletti, L., Perez Garcia, A. M., et al. 2017, arXiv e-prints, arXiv:1705.05693, doi: 10.48550/arXiv.1705.05693
- Mayor, M., Marmier, M., Lovis, C., et al. 2011, arXiv e-prints, arXiv:1109.2497, doi: 10.48550/arXiv.1109.2497
- McClure, M. 2009, ApJL, 693, L81, doi: 10.1088/0004-637X/693/2/L81
- Megeath, S. T., Gutermuth, R., Muzerolle, J., et al. 2012, AJ, 144, 192, doi: 10.1088/0004-6256/144/6/192
- Mulders, G. D., Pascucci, I., Ciesla, F. J., & Fernandes,
  R. B. 2021, ApJ, 920, 66, doi: 10.3847/1538-4357/ac178e
- Najita, J. R., & Kenyon, S. J. 2014, MNRAS, 445, 3315, doi: 10.1093/mnras/stu1994
- Ochsenbein, F., Bauer, P., & Marcout, J. 2000, A&AS, 143, 23, doi: 10.1051/aas:2000169
- Offner, S. S. R., Taylor, J., Markey, C., et al. 2022, MNRAS, 517, 885, doi: 10.1093/mnras/stac2734
- Oliveira, I., Merín, B., Pontoppidan, K. M., & van Dishoeck, E. F. 2013, ApJ, 762, 128, doi: 10.1088/0004-637X/762/2/128
- Oliveira, I., Merín, B., Pontoppidan, K. M., et al. 2009, ApJ, 691, 672, doi: 10.1088/0004-637X/691/1/672
- Paneque-Carreño, T., Pérez, L. M., Benisty, M., et al. 2021, ApJ, 914, 88, doi: 10.3847/1538-4357/abf243
- Pascucci, I., Testi, L., Herczeg, G. J., et al. 2016, ApJ, 831, 125, doi: 10.3847/0004-637X/831/2/125
- Paxton, B., Bildsten, L., Dotter, A., et al. 2011, ApJS, 192, 3, doi: 10.1088/0067-0049/192/1/3
- Paxton, B., Cantiello, M., Arras, P., et al. 2013, ApJS, 208, 4, doi: 10.1088/0067-0049/208/1/4
- Paxton, B., Marchant, P., Schwab, J., et al. 2015, ApJS, 220, 15, doi: 10.1088/0067-0049/220/1/15
- Pecaut, M. J., & Mamajek, E. E. 2013, ApJS, 208, 9, doi: 10.1088/0067-0049/208/1/9
- Reback, J., Jbrockmendel, McKinney, W., et al. 2022, pandas-dev/pandas: Pandas 1.4.4, v1.4.4, Zenodo, doi: 10.5281/zenodo.7037953
- Ribas, Á., Espaillat, C. C., Macías, E., & Sarro, L. M. 2020, A&A, 642, A171, doi: 10.1051/0004-6361/202038352
- Ribas, Á., Espaillat, C. C., Macías, E., et al. 2017, ApJ, 849, 63, doi: 10.3847/1538-4357/aa8e99
- Ribas, Á., Macías, E., Weber, P., et al. 2023, A&A, 673, A77, doi: 10.1051/0004-6361/202245637
- Rilinger, A. M., Espaillat, C. C., Xin, Z., et al. 2023, ApJ, 944, 66, doi: 10.3847/1538-4357/aca905

- Roman-Zuniga, C. G., Kounkel, M., Hernandez, J., et al. 2023, VizieR Online Data Catalog: Stellar properties in SFRs from SDSS APOGEE-2 (Roman-Zuniga+, 2023), VizieR On-line Data Catalog: J/AJ/165/51. Originally published in: 2023AJ....165...51R
- Rota, A. A., Manara, C. F., Miotello, A., et al. 2022, A&A, 662, A121, doi: 10.1051/0004-6361/202141035
- Ruíz-Rodríguez, D., Ireland, M., Cieza, L., & Kraus, A. 2016, MNRAS, 463, 3829, doi: 10.1093/mnras/stw2297
- Ruíz-Rodríguez, D., Cieza, L. A., Williams, J. P., et al. 2018, MNRAS, 478, 3674, doi: 10.1093/mnras/sty1351
- Savvidou, S., & Bitsch, B. 2024, arXiv e-prints, arXiv:2407.08533, doi: 10.48550/arXiv.2407.08533
- Segura-Cox, D. M., Schmiedeke, A., Pineda, J. E., et al. 2020, Nature, 586, 228, doi: 10.1038/s41586-020-2779-6
- Serna, J., Hernandez, J., Kounkel, M., et al. 2023, VizieR Online Data Catalog: TESS obs. & rotational periods of T Tauri in Orion (Serna+, 2021), VizieR On-line Data Catalog: J/ApJ/923/177. Originally published in: 2021ApJ...923..177S
- Shakura, N. I., & Sunyaev, R. A. 1973, A&A, 24, 337
- Shu, F. H., Adams, F. C., & Lizano, S. 1987, ARA&A, 25, 23, doi: 10.1146/annurev.aa.25.090187.000323
- Skrutskie, M. F., Cutri, R. M., Stiening, R., et al. 2006, AJ, 131, 1163, doi: 10.1086/498708
- Taylor, M. B. 2005, in Astronomical Society of the Pacific Conference Series, Vol. 347, Astronomical Data Analysis Software and Systems XIV, ed. P. Shopbell, M. Britton, & R. Ebert, 29
- Testi, L., Natta, A., Manara, C. F., et al. 2022, A&A, 663, A98, doi: 10.1051/0004-6361/202141380

- Thorngren, D. P., Fortney, J. J., Murray-Clay, R. A., & Lopez, E. D. 2016, ApJ, 831, 64, doi: 10.3847/0004-637X/831/1/64
- Throop, H. B., & Bally, J. 2008, in AAS/Division of Dynamical Astronomy Meeting, Vol. 39, AAS/Division of Dynamical Astronomy Meeting #39, 17.01
- Tychoniec, L., Manara, C. F., Rosotti, G. P., et al. 2020, A&A, 640, A19, doi: 10.1051/0004-6361/202037851
- van der Marel, N., Verhaar, B. W., van Terwisga, S., et al. 2016, VizieR Online Data Catalog, J/A+A/592/A126, doi: 10.26093/cds/vizier.35920126
- van Terwisga, S. E., Hacar, A., van Dishoeck, E. F., Oonk, R., & Portegies Zwart, S. 2022, A&A, 661, A53, doi: 10.1051/0004-6361/202141913
- van Terwisga, S. E., van Dishoeck, E. F., Cazzoletti, P., et al. 2019, A&A, 623, A150, doi: 10.1051/0004-6361/201834257
- Villenave, M., Ménard, F., Dent, W. R. F., et al. 2021, A&A, 653, A46, doi: 10.1051/0004-6361/202140496
- Virtanen, P., Gommers, R., Oliphant, T. E., et al. 2020, Nature Methods, 17, 261, doi: 10.1038/s41592-019-0686-2
- Vousden, W. D., Farr, W. M., & Mandel, I. 2016, MNRAS, 455, 1919, doi: 10.1093/mnras/stv2422
- Wenger, M., Ochsenbein, F., Egret, D., et al. 2000, A&AS, 143, 9, doi: 10.1051/aas:2000332
- Williams, J. P., Cieza, L., Hales, A., et al. 2019, ApJL, 875, L9, doi: 10.3847/2041-8213/ab1338
- Williams, J. P., & Cieza, L. A. 2011, ARA&A, 49, 67, doi: 10.1146/annurev-astro-081710-102548
- Xin, Z., Espaillat, C. C., Rilinger, A. M., Ribas, Á., & Macías, E. 2023, ApJ, 942, 4, doi: 10.3847/1538-4357/aca52b
- Yao, Y., Meyer, M. R., Covey, K. R., Tan, J. C., & Da Rio, N. 2018, ApJ, 869, 72, doi: 10.3847/1538-4357/aaec7a

#### APPENDIX

#### A. SAMPLE SELECTION CRITERIA

The original samples of 320 Serpens sources (Anderson et al. 2022) and 873 L1641/L1647 sources (van Terwisga et al. 2022) are reduced to samples of 23 and 188 objects, respectively, after considering the following selection criteria:

• The sources must belong to the Serpens or L1641/L1647 star-forming regions.

Anderson et al. (2022) selected their sources by inspecting the Spitzer c2d and Gould Belt surveys, which consisted of 1546 YSOs identified towards the Serpens region. They selected a sample of 320 objects for their ALMA survey by choosing only those sources with infrared slopes less than 1.6 (representative of Class I, Flat, and Class II YSOs; Williams & Cieza 2011). In their observation results table (Table 1; Anderson et al. 2022), the G flag is employed to denote sources that are situated beyond the probable distance range of Serpens members. This reduces the reported observed sample from 320 to 302 likely members of the Serpens region. For further information regarding the process of membership selection, we refer the reader to Dunham et al. (2015) and Anderson et al. (2022).

The SODA sample from van Terwisga et al. (2022) consists of 873 objects that belong to the L1641 and L1647 regions, located in the Orion A cloud at < -6° deg in declination. These were selected from the *Spitzer* survey of YSOs in the Orion A and B molecular clouds performed by Megeath et al. (2012). The 41 objects in L1641, already modeled in Rilinger et al. (2023), are included in our sample (see Section 4.2). For consistency, we use the same source identifier as in Megeath et al. (2012) and van Terwisga et al. (2022), abbreviating with [MGM2012] and the number of the object in the catalog.

• The sources must be identified as Class II.

For the Serpens sample, we used the YSO class flag included in the Anderson et al. (2022) results table (based on the infrared slope value characteristic of a Class II object; Williams & Cieza 2011), reducing the sample to 235 objects. The van Terwisga et al. (2022) sample is comprised entirely of Class II YSOs from Megeath et al. (2012), so

no sources were discarded from the L1641/L1647 sample based on this criterion.

- The sources must have been detected by ALMA. Non-detections were included in the Anderson et al. (2022) table for completeness. Discarding these sources reduces the sample to 182 objects, while for the L1641/L1647 sample, we only selected resolved sources, reducing the number of objects to 502.
- The sources must have at least two 2MASS measurements, two mid-IR (WISE or cd2) measurements, and one (sub)mm (ALMA) measurement.
   A photometric point at ≥ 500µm ensures coverage

A photometric point at  $\geq 500\mu m$  ensures coverage up to the (sub)mm regime, ideal for constraining the disk mass. As our models have many parameters, we require a minimum number of photometric points to obtain an appropriate fit and prevent degeneracies at the moment of SED modeling. 2MASS provides information on stellar properties, while the mid-IR traces the disk's emission. Applying this criterion does not alter the size of the Serpens sample, as all sources have measurements; meanwhile, the L1641/L1647 sample is affected and reduced to 442 objects.

• The source is not known to be a transitional disk (TD), have a flat spectrum, or be in a binary/multiple system.

The ANN omits TDs in its training sample (Ribas et al. 2020). Binary and multiple systems are avoided since they cause confusion when compiling their SED data, and in cases of low spatial resolution, this leads to inaccurate photometry. We discarded sources with companions <1000 au, based on the literature, as binarity can impact protoplanetary disk properties, structure, and evolution (e.g., Artymowicz & Lubow 1994; Cieza et al. 2009; Kraus et al. 2012; Harris et al. 2012; Kounkel et al. 2016; Ruíz-Rodríguez et al. 2016; Cox et al. 2017; Akeson et al. 2019; Barenfeld et al. 2019; Cazzoletti et al. 2019; Villenave et al. 2021; Rota et al. 2022). We refer the reader to Offner et al. (2022), for a recent review on the effects of binarity on disk systems.

For the Serpens sample, we identified objects as TDs following van der Marel et al. (2016), and used the provided flag  $\mathbf{T}$  in Anderson et al. (2022),

or used visual inspection of the SED to identify a "dip" in the mid-IR range (e.g., 2MASS J18300893+0047219 shows a SED characteristic of a TD). This reduces the Serpens sample to 163 objects.

For the L1641/L1647 sample, we consulted the Kim et al. (2013) infrared spectroscopic survey of Orion A on transitional disks, finding 19 objects in our sample identified as a type of TD (ranging from classical TD, weak-excess TD, and pre-TD). From the Fang et al. (2013) L1641 study, we identified 23 objects as TD or Flat spectrum. Visually we identified and discarded [MGM2012] 128, 828, and 1066 as they show a "dip" around the mid-IR range, characteristic of the SED structure of a TD. From the Fang et al. (2009) catalog, six objects are identified as TD: [MGM2012] 339, 365, 377, 395, 481, 971. We exclude five objects associated with extended millimeter-continuum emission from the envelope ([MGM2012] 56, 227, 421, 714, and 975; van Terwisga et al. (2022)). We also discard compact (visual) systems with companions within <10" (4000 au) (e.g., [MGM2012] 129, 754, 1000, 1090, and 1094). This reduces the L1641/L1647 sample to 381 objects.

• The sources must not have a (sub)mm measurement within 2".5 of another (sub)mm detection of at least  $3\sigma$ .

For the Serpens sample, we used the provided flag **B** in Anderson et al. (2022), which indicates that an object is detected in a binary system, with a  $3\sigma$  mm detection within 2".5 (~1000 au) of the central source. This reduces the sample to 162 after discarding 2MASS J18311972-0201115. For the L1641/L1647 sample, we discarded one class II source ([MGM2012] 512) associated with extended millimeter-continuum emission (Grant et al. 2021; Cacciapuoti et al. 2024), reducing the sample to 380 objects.

 $\bullet$  The sources must have an ALMA detection of at least  $3\sigma$ 

This reduces the Serpens sample to 70 objects while it keeps the L1641/L1647 sample unchanged.

• The sources must display good *Gaia* astrometric quality.

To satisfy this, we select sources with *Gaia* DR3 astrometry. This reduces the Serpens sample to 42 sources. Although 2MASS 18314182-0207590 is included as a *Gaia* DR3 object, it is discarded

as it does not have parallax values. We follow Lindegren et al. (2021), which recommends the use of the renormalized unit weight error (RUWE, the uncertainty in measurements) to evaluate the quality of the astrometric solution. We apply two criteria for good astrometric fits: a parallax error below 20%, and a RUWE <1.4. This reduces the Serpens sample to 29 sources, while the L1641/L1647 sample is reduced to 205 objects.

• The sources must be T Tauri stars.

The ANN training is optimized with DIAD models that cover an estimated stellar mass in the range from 0.1 -  $2.0~M_{\odot}$  (Ribas et al. 2020). This generally corresponds to the range of masses associated with T Tauri stars, and so we discard objects classified as Herbig Ae/Be stars to ensure that no stars outside the stellar mass range covered by the ANN are included. From the Serpens sample, 2MASS J18295533+0049391 was discarded as it is identified as a Herbig Ae/Be star in Oliveira et al. (2009). This results in the reduction of the Serpens sample to 28 objects. In the L1641/L1647 sample, we identified four sources as Herbig Ae/Be following Guzmán-Díaz et al. (2021): [MGM2012] 612, 760, 838, 1031. This reduces the L1641/L1647 sample to 201 objects.

• The sources must have stellar parameters in the literature.

Stellar parameters are listed in Tables 1 & 2. For Serpens, we use Harvey et al. (2007); Oliveira et al. (2009, 2013); Erickson et al. (2015) for the star's mass, radius, effective temperature, spectral type, and visual extinction. For the L1641/L1647 sources, we use Fang et al. (2009, 2013, 2018); Hsu et al. (2012, 2013); da Rio et al. (2016); Kounkel et al. (2016); Kim et al. (2016); Yao et al. (2018); Roman-Zuniga et al. (2023); Serna et al. (2023); Abdurro'Uf & et al. (2023). Tables 1 & 2 also include parallaxes and their respective error values obtained from *Gaia* DR3. These are all parameters later used as priors for the ANN.

After inspecting all objects, we found that 5 objects from Serpens did not have parameters available in any catalog: [2MASS] 18274937-0353404, 18314002-0205339, 18314616-0153493, 18314791-0211559, 18325715-0245162. For L1641/L1647, 13 objects do not have available parameters: [MGM 2012] 102, 108, 121, 132, 146, 152, 168, 171, 229, 249, 260, 683, 974. These sources were dis-

carded, reducing the Serpens sample to 23 and the L1641/L1647 sample to 188.

# B. PRIORS VS POSTERIORS

An evaluation of the consistency between the stellar parameters  $M_*$ ,  $R_*$ , parallax, and  $T_{\text{eff}}$  (as listed in Tables 1 and 2 and used as priors in our modeling) and their corresponding posterior distributions (in Tables 4 and 5) is performed to check for sources where our modeling suggests significant discrepancies with literature measurements. Figures 12 and 13 illustrate the comparison between existing literature measurements and the posterior probability distributions obtained via the ANN. As expected, the posterior distribution for the disks' stellar parameters are in general consistent with literature measurements. This suggests that the literature values used as priors are not problematic, and our methodology allows us to incorporate the uncertainty on these stellar parameters in the posterior distributions of the disk parameters (Ribas et al. 2020).

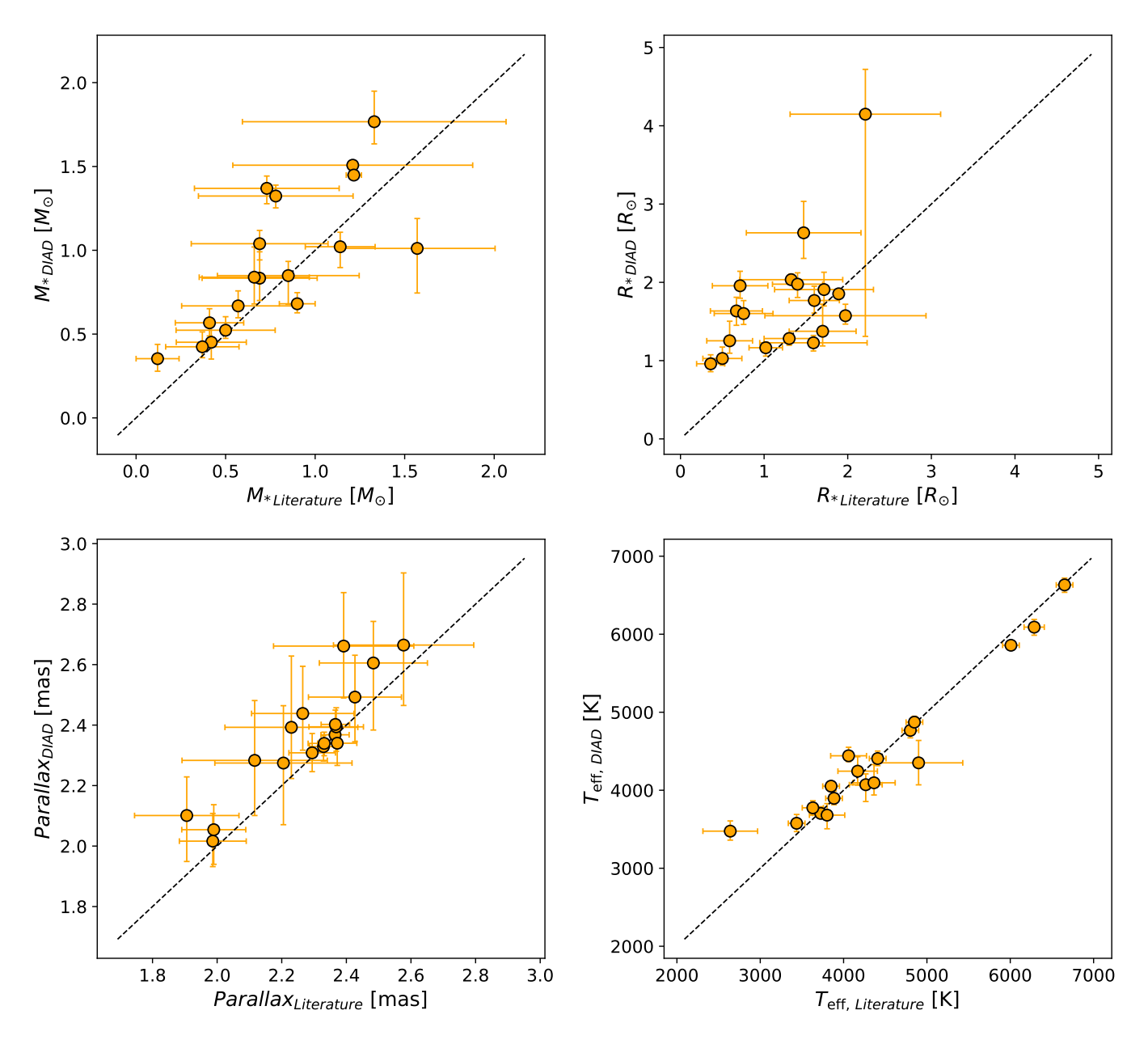


Figure 12. Comparison between the existing literature prior values and the posterior value estimations derived from the ANN analysis of the Serpens disks. The dotted black line denotes a perfect correlation (one-to-one fit) between the values.

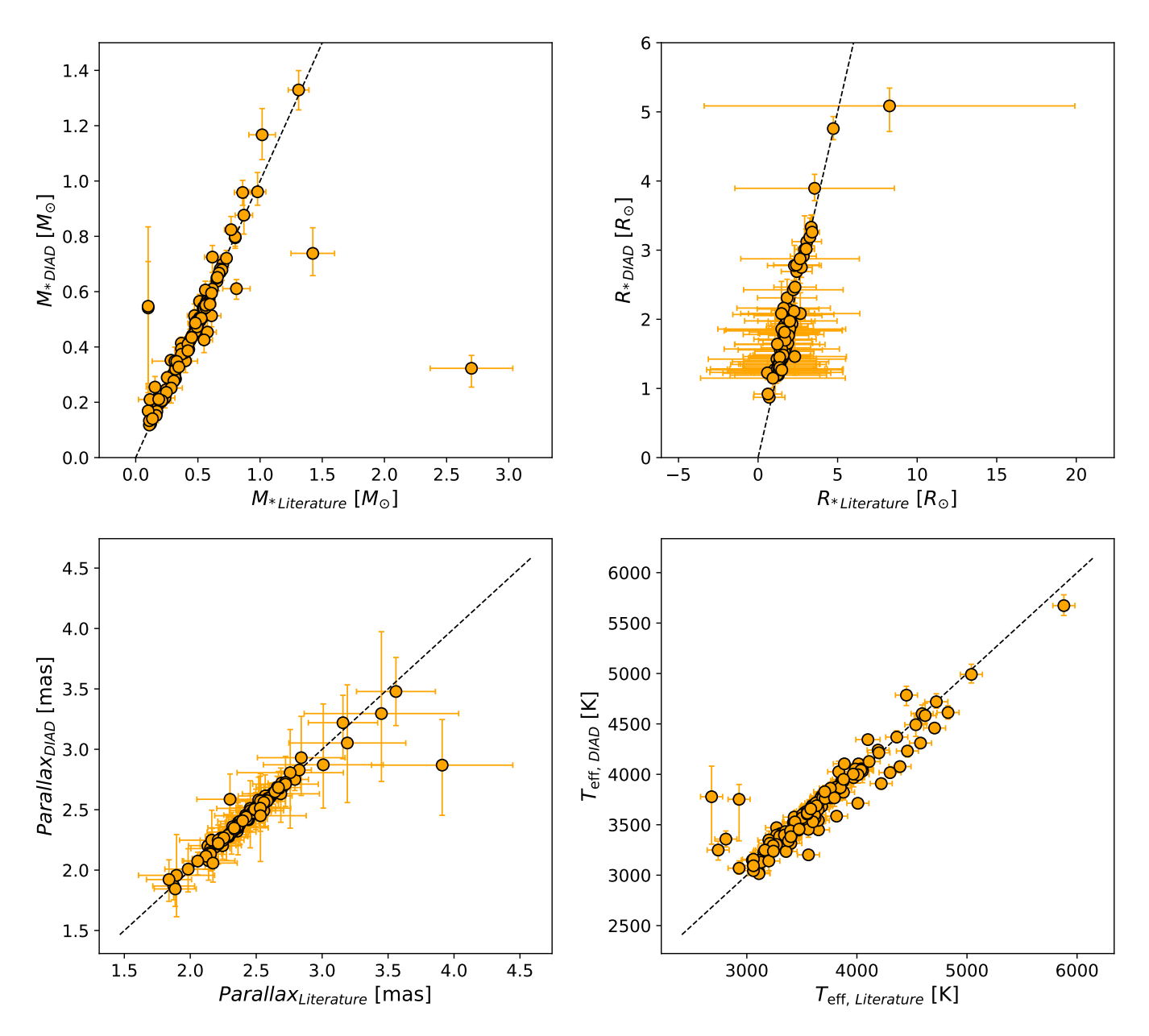


Figure 13. Comparison between the existing literature prior values and the posterior value estimations derived from the ANN analysis of the L1641 & L1647 disks. The dotted black line denotes a perfect correlation (one-to-one fit) between the values.